AN EXPERIMENTAL INVESTIGATION OF CIRCULATION CONTROL FLOW FIELDS USING HOLOGRAPHIC INTERFEROMETRY

CR 166482

by

W. D. Bachalo

Aerometrics, Inc.

for

NASA Ames Research Center

October 1982

TABLE OF CONTENTS

		Page
1.0	INTRODUCTION	1
2.0	EXPERIMENTAL PROCEDURE	6
	2.1 Description of the Model	6
	2.2 Holographic Interferometry	8
	2.3 Data Reduction	14
3.0	RESULTS AND DISCUSSION	16
4.0	SUMMARY AND CONCLUSIONS	63
	REFERENCES	65

1.0 INTRODUCTION

This report describes the experiments conducted on flow fields produced by a circulation control airfoil utilizing the Coanda effect at the trailing edge. The Coanda effect occurs when a high-velocity fluid jet emits tangentially from a surface slot. The jet attaches itself to the surface because of the reduced static pressure it produces. As a result of this low static pressure produced by the jet adjacent to the wall, the jet will remain attached even while executing a relatively sharp turn about the airfoil trailing edge. It is apparent that the lowered static pressure produced by the jet velocity must balance the centrifugal force of the jet. That is, $dp/dr = \rho V^2/R$ where R is the radius of curvature of the airfoil trailing edge, and V is the jet mean velocity. The point at which the jet separates from the surface is determined by the momentum of the jet being reduced to the point wherein opposing centrifugal and lower surface-flow momentum forces are balanced.

The jet also entrains the surrounding fluid which serves to keep the airfoil boundary layer attached. In addition to the momentum added to the boundary layer by the jet, the reduced static pressure presents a strong favorable pressure gradient to the boundary layer. This further assists in maintaining attached flow well-around the typically blunt trailing edges of circulation control airfoils.

Circulation control airfoils, unlike conventional airfoils with sharp trailing edges, have either round or elliptical trailing-edge shapes. The rounded trailing edge allows the rear stagnation point to move. Movement of the rear stagnation point is controlled by the relative blowing momentum and the Mach and Reynolds numbers of the flow

field. Obviously, as the stagnation point is moved further around the trailing edge, an effective camber is introduced and the lift is increased.

There is a great deal of interest in the application of circulation control concepts to helicopters. In fact, Coanda blowing has already been tested on the tail boom of a helicopter in an effort to replace the sometimes hazardous tail rotor. Of greater interest is the use of Coanda blowing (both forward and rear edge) on the rotor. Conventional rotor blades suffer from stalled retreating blades in high-speed forward flight, complicated mechanical control systems and vibration. It has been determined that with both forward and rear edge blowing, lift can be produced even with areas of reversed flow on the rotor blade. Control of the aircraft could be easily accomplished by valve adjustments to the blowing.

Because a high lift is generated at lower tip speeds, the rotor noise generated by conventional rotors may also be reduced. The most intense rotor noise is caused by the shock that is formed on the advancing blade and which subsequently leaves the blade as the rotor moves around to the retreating direction. Presumably, with high Coanda blowing, the rotor flow could be kept subcritical or at least at a level where the shock strength is reduced relative to conventional rotors.

A good current list of references on work conducted in wall jets is given in reference 1. Englar[2,3] has conducted research on a number of circulation control airfoil configurations at subsonic and transonic speeds. Model configurations included a pure elliptical shape utilizing Coanda blowing and a model using jet flap blowing. In these studies, the pressure distributions, lift, and drag were measured to evaluate the

performance of the various configurations. The performance of a rounded trailing-edge model showed the best performance for Mach numbers below 0.55. However, at higher Mach numbers the Coanda jet apparently detached resulting in a rapid deterioration of performance. The elliptical trailing-edge shape with its larger radius downstream of the slot was able to withstand jet detachment to a Mach number of 0.7. At these Mach numbers, maximum lift-to-drag ratios of 22 at $C_\ell = 0.44$ were attained. Englar found that the jet flap was inferior in all respects to the tangentially blown configurations. In his report, Englar recognized the importance of understanding the phenomenon of high-speed Coanda jet detachment and its effects upon the upper surface shock-boundary-layer interaction and also the effect of the underexpanded supersonic jet that is produced at certain blowing conditions.

A subsequent report[3] treated the jet flow in more detail. This study involved a 20% thick modified elliptic profile using high Coanda jet velocities. A hot-film anemometer was used to obtain shear stress measurements over a range of slot heights and jet total pressures. Jet speeds ranging from subsonic to supersonic were tested. It was found that even at jet Mach numbers as high as 1.3, deleterious jet detachment was not an operational problem. However, the jet height was found to significantly affect the performance. The higher kinetic energy of the reduced jet height resulted in better Coanda turning and hence, lift augmentation.

Shear-stress measurements were used to obtain information of the transitional behavior of the jet and where jet separation occurred. The shear-stress measurements indicated a rapid drop and then a rise in skin friction downstream of the jet slot as the jet boundary layer went through laminar-to-turbulent transition. These measurements were also

used to show that the jet peak shear stress and separation point move downstream with increased duct pressure even after jet chocking is reached.

Useful suggestions were made by Englar regarding future research. Because of problems experienced with wind-tunnel blockage, it was suggested that similar investigations be conducted in a tunnel with a much greater height-to-chord ratio. Also, the need for extensive flow visualization using optical diagnostics was strongly recommended.

Work conducted by Ottensoser[4] investigated the feasibility of blowing at both the leading and trailing edges. He found the existence of a leading-edge slot did not effect the performance except at higher angles of attack. When simultaneous blowing of both the leading and trailing edges were used, a decrease in the lift-to-drag and augmentation ratios occurred along with an increase in the positive pitching moment as compared to rear blowing only.

A study by Abramson[5] addressed the effects of airfoil camber on the aerodynamic characteristics of a two-dimensional circulation control airfoil at subsonic flow speeds. It was found that the initiation of blowing reduced the otherwise high drag. Preliminary comparisons of the results from two-dimensional potential flow calculations to the experimental data were made to estimate the extent of spanwise nonuniformity in the flow. The good agreement obtained indicated that the flow was quasi-two-dimensional.

Wood[1] recently conducted a comprehensive investigation on the aerodynamics of a 20% circulation control aerofoil with an elliptic cross section having both leading and trailing edges blowing. These experiments were performed in a 2-m by 1.5-m low-speed facility with a maximum flow

speed of approximately 50 m/sec. A model of chord length equal to 59.4 cm and leading and trailing-edge radii of 5.08 cm was used. Hot-wire and split-film anemometers were used to obtain detailed mean velocity and turbulence intensity profiles at various blowing rates. Data obtained clearly show the effect of the jet interaction with the airfoil boundary layer and the corresponding relaxation of the turbulence intensity upstream of the jet.

Because there have been very few tests on circulation control airfoils at transonic speeds, the present investigations were conducted to provide data in this very important regime. The dynamic pressures and presence of shocks on the airfoil can be expected to affect the performance. Also, the effects of Reynolds number and Mach number have not been determined. Thus, in the present experiments a series of tests were planned to cover a range of Mach numbers, angles of attack, and Reynolds numbers. Surface pressure measurements, interferometry, and laser Doppler velocimetry were utilized in the investigation. Also, information on the jet behavior was desired.

The present report will cover the application of holographic interferometry to obtain both visualization and quantitative data on the flow field. In the following sections a brief description of the flow model and measurement techniques will be given. Following this, the data reduction procedure, results, and interpretation will be presented.

2.0 EXPERIMENTAL PROCEDURE

2.1 Description of the Model

The present investigation was conducted on a 15.2 cm (6 in.) chord model having a 21.2% thickness-to-chord ratio and 3% camber. A single blowing slot of height 0.30 mm ± 0.08 mm located at 96.2% chord was used. The model is made up of four sections as shown in figure 1. There were a total of 91 pressure taps on the model. Of these, 59 were positioned along the centerline with 17 upper leading section, 17 on the lower, 7 on the upper trailing-edge section, and 18 on the lower trailing-edge section of the model. Two of these are located under the slot lip.

Although the span-to-chord ratio was only 4, no means was incorporated to control the sidewall boundary layers. It should be anticipated that when testing under high-lift conditions, the effect of the tunnel upper and lower walls will also produce a constraint on the streamline curvature. This will produce an apparent increase in the effective camber of the model.

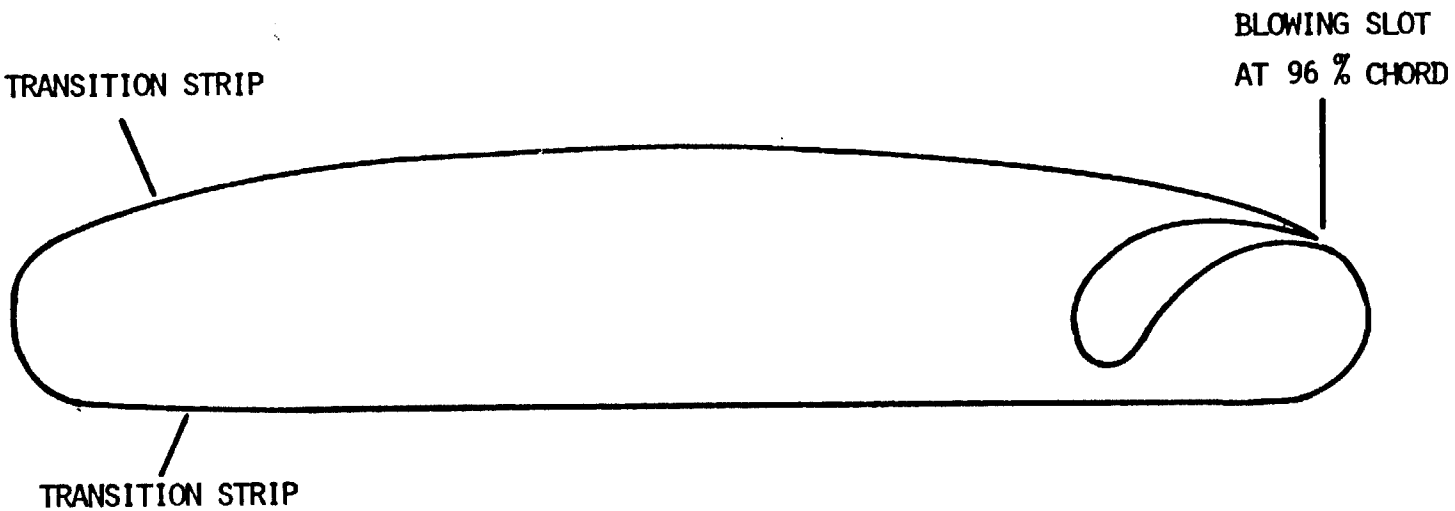

15.2 cm chord

21.2% Thickness ratio

3% Camber

Figure 1.- Schematic of the circulation control model.

2.2 Holographic Interferometry

Interferometry which utilizes the mixing of two coherent waves for the purpose of measuring the distortion in one of the waves, has been used in small-scale wind tunnels and is well-understood. The introduction of holography as an intermediary to store the light-wave information allows a great deal of versatility in the use of the technique and significantly extends the possible applications.

With holography, the amplitude and phase distribution of a light wave passing through the flow field at some instant of time can be stored and later reconstructed for comparison to waves formed at other conditions. This allows the storage of several test conditions for later comparison and analysis outside of the test facility. In addition to the interferometry techniques, the shadowgraph and Schlieren flow visualization techniques are also available. The ability to reconstruct the light field outside of the wind tunnel allows a much greater flexibility in spatial filtering and photographing the images.

Transonic flows are especially suitable to the application of interferometry since compressibility occurs but the density changes are not all stepwise through shocks as in supersonic flow. In addition, the shocks present in the transonic flow fields are weak so that the entire flow field can be assumed to be isentropic. Thus, the interference fringes are at the same time a mapping of the constant density and the flow speed contours. These data can be readily reduced, with the use of other wind-tunnel conditions, to the surface static pressure and viscous layer temperature profiles.

A Quanta Ray DCR-1 Nd:YAG laser is used in the Ames 2-ft by 2-ft transonic facility's holographic interferometer as the light source. This

laser is capable of producing pulse rep rates between 2/sec and 20/sec at up to 80 mJ of energy in the green line (0.532 μm). Because of the high rep rate capability, a separate HeNe laser is not required for aligning the optics as in the case of a pulsed ruby laser system.

The hologram recording system is composed of a transmitting and receiving components (figs. 2 and 3), connected by two optical paths for the object and reference beams. The Quanta Ray DCR-1 pulsed Nd:YAG laser used in the system produces a beam that has a so-called "donut" intensity distribution due to the laser's unstable resonator configuration. Thus, the first elements in the system consisting of lens L1 and a spatial filter of 150-μm aperture is used to produce a smooth beam intensity distribution. The beam is then divided into two paths with a beam splitter (B.S.), shown on figure 2.

The object beam is reflected from the beam splitter and expanded with lens L3 to overfill the Schlieren mirror. Because the foci of L3 and the Schlieren mirror coincide, a collimated beam is formed and transmitted through the test section. The object beam is 46 cm in diameter and is received and refocussed to the receiver stage. Lens L6 is used to collimate the object beam to an appropriate size for recording at the holographic plate (fig. 3).

The reference beam is directed through the beam splitter and down into a trench passing under the wind tunnel. Lens L2 is used to control the size of the reference beam at the receiver stage. Lenses L4 and L5 are used to expand and collimate the reference beam to 90 mm in diameter which then also falls on the holographic plate.

A 4-in. by 5-in. film holder is used to hold the high-resolution holographic film plates for recording the information. When using the

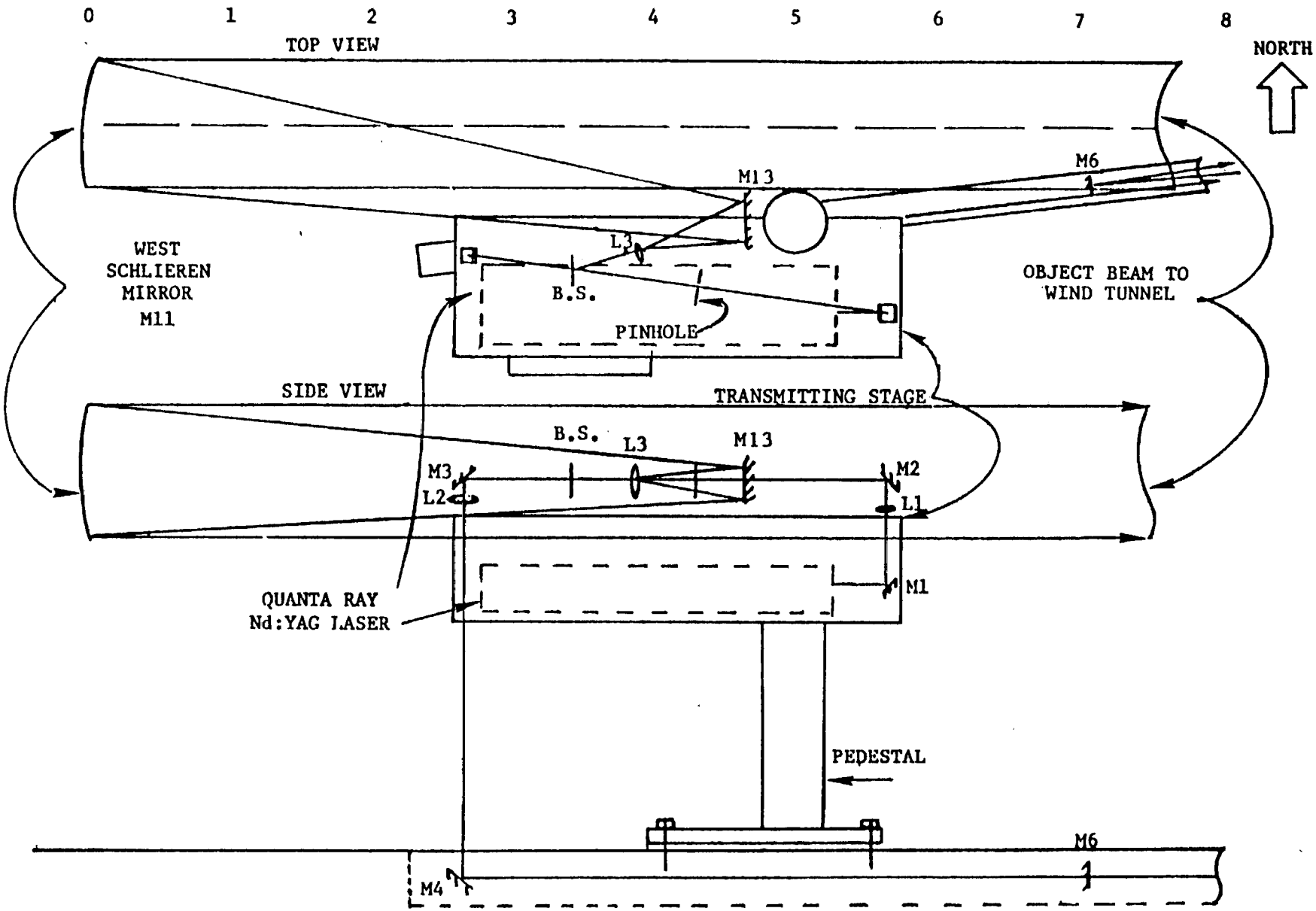

Figure 2.- Transmitting stage schematic of the 2- by 2-ft holographic interferometer.

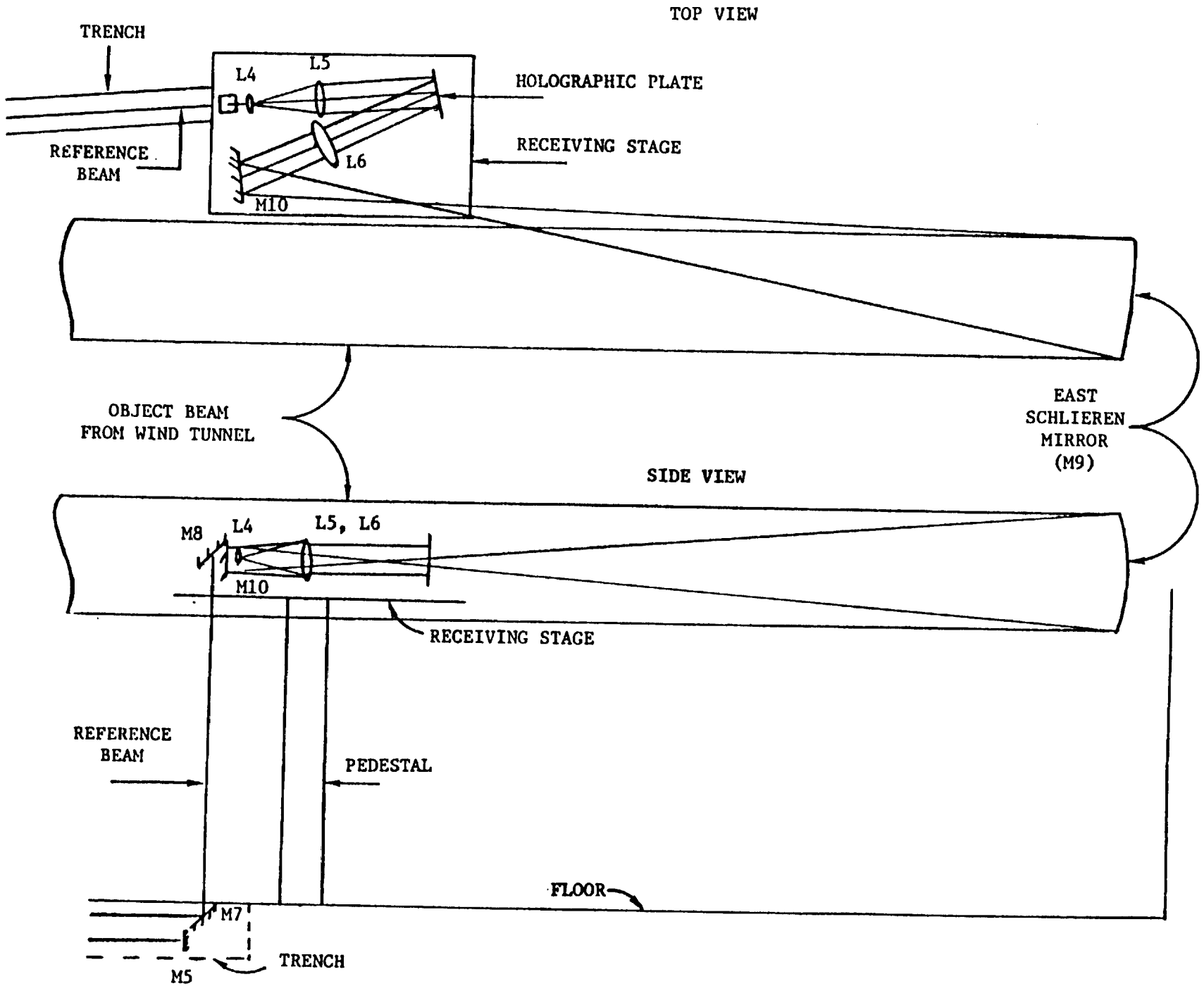

Figure 3.- Receiving stage schematic of the 2- by 2-ft holographic interferometer.

dual plate interferometry technique, holograms are recorded with no flow in the tunnel (reference condition) and subsequent plates are recorded at the test conditions.

After processing the exposed film, the reconstruction system shown in figure 4 allows viewing and photographing the aerodynamic information. The dual plate holder is used to position the reference and test plates to produce interference between the two reconstructed object waves. Lens 7 images the test section onto the film plane of a 4-in. by 5-in. camera and produces a beam diameter of suitable size for recording on 4 by 5 sheet film.

One major difficulty when utilizing the dual plate technique arises when the density of the entire flow field is disturbed. In this case, it is difficult if not impossible to ascertain when the interferometer is aligned to the infinite fringe condition. That is, to the case wherein fringes only occur as a result of changes in the flow density. This condition occurs in most airfoil tests. Fortunately, a knowledge of the transonic flow characteristics and other alignment criteria has led to reconstructed interferograms producing good agreement with other measured data.

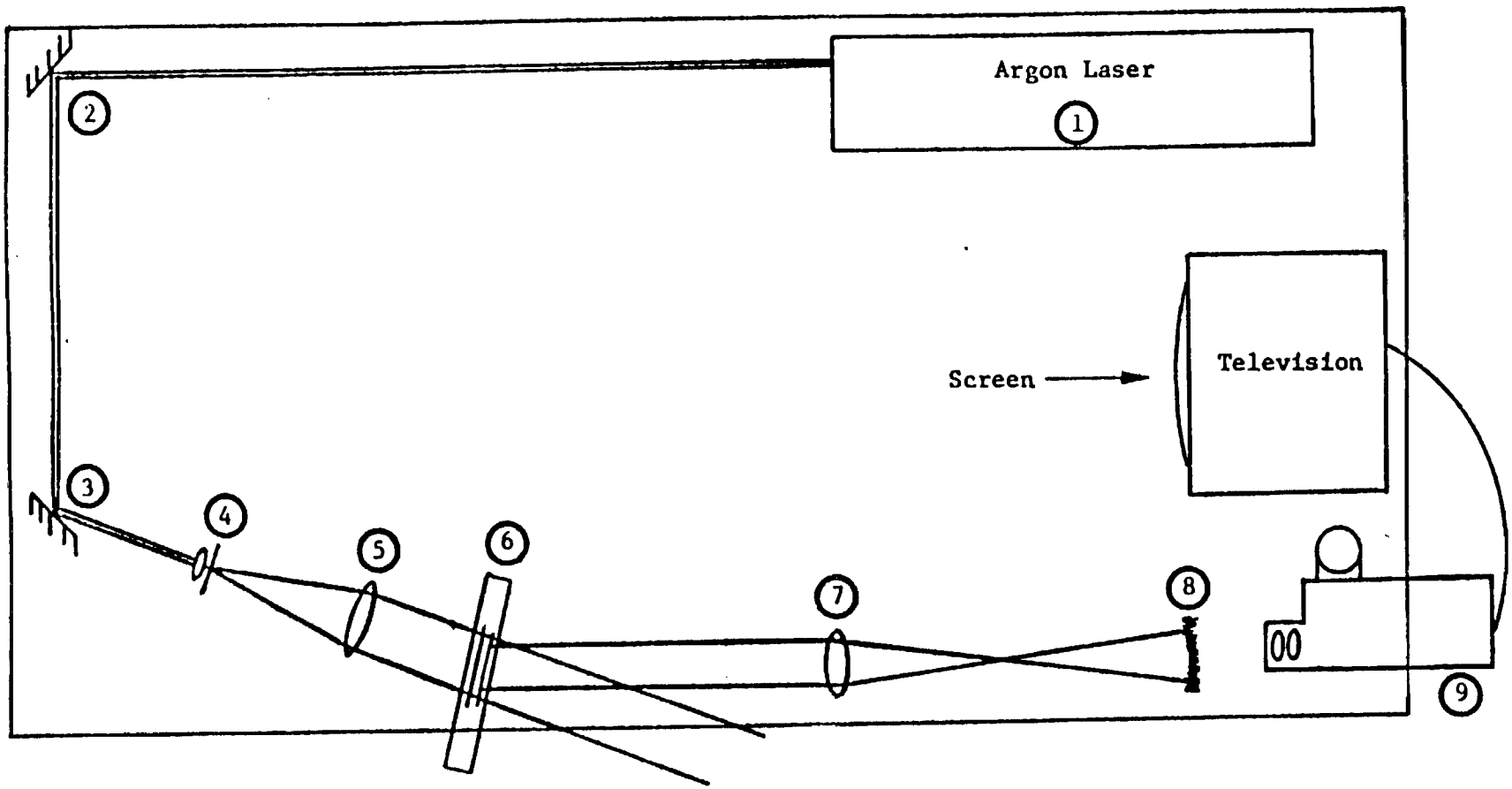

1. Argon Laser
2 - 3. 1 or 2-inch diameter dielectric coated mirrors reflective @ 45° incidence @ λ = 5320 Å
4. Lens pinhole assembly
5. Collimating lens - ϕ = 110 mm diameter, fl = 240 mm Rolyn #20.1325
6. Dual plate holder
7. o imaging lens - ϕ = 110 mm diameter, fl = 240 mm, Rolyn #20.1325
8. Ground glass viewing screen
9. Camera head

Figure 4.- Reconstruction system schematic.

2.3 Data Reduction

Obtaining quantitative results from the interferograms is straightforward for two-dimensional flows. The pathlength through the wind tunnel in the present case was two feet so the density changes at the test flow Mach numbers was sufficient to produce an optimum number of interference fringes in the infinite fringe mode. Using the infinite fringe mode has the advantage of the fringes producing a direct mapping of the constant density contours which in turn, map the Mach contours.

Evaluation of the density change per fringe can be determined using the following relationships. In an inhomogeneous density test field the phase shift of the light wave is

$$\left(\frac{\Delta\phi}{2\pi}\right) = \frac{1}{\lambda} \int_{\zeta}^{\zeta_1} [n(x,y) - n_o]dz$$

where λ is the laser wavelength and n is the index of refraction. When the interferometer is aligned in the infinite fringe mode, the equation of the fringes is

$$\int_{\zeta}^{\zeta_1} [n(x,y) - n_o]dz = N\lambda$$

where N is an integer. Applying the Gladstone-Dale Constant relating phase variation to density, the integrated relationship is

$$\rho(x,y) = \rho_o + \frac{N\lambda}{KL}$$

The constant values in the present case are:

$$L = 609.6 \text{ mm}$$

$$\lambda = 0.532 \ \mu\text{m}$$

$$K = 0.226 \ (\text{gm/cm}^3)^{-1}$$

$$\frac{\lambda}{KL} = \frac{0.532 \times 10^{-3} \text{ mm}}{0.226 \ (\text{gm/cm}^3)^{-1} \ 609.6 \text{ mm}}$$

Combining the constants and adjusting for the wall boundary layers result in:

$$\rho_1 - \rho_0 = 2.46 \times 10^{-4} \ \frac{\text{lbm/ft}^3}{\text{fringe}}$$

It remains to identify a particular fringe to be used as the reference with its corresponding density. This can be done in several ways. If there is a region of undisturbed flow in the field of view, the wind-tunnel conditions can be used. Unfortunately, this is not generally the case. Instead, a surface pressure measurement can be converted to density by using the total temperature, T_o, and the total pressure, P_o. Another independent reference can be obtained from the inviscid flow velocity measured with the laser velocimeter.

Some representative boundary layer and wake profiles have also been measured. These data were obtained under the usual assumption that the static pressure does not vary in a direction normal to the surface and that the stagnation temperature is constant. Manual counting of the fringes allowed an estimated resolution of about 0.3 of a fringe width and a spatial resolution of ±0.10 mm using a metric scale and a loupe.

The viscous flow speeds were derived using the Crocco relationship given by

$$\frac{T}{T_e} = 1 + r \frac{\gamma - 1}{2} M_e^2 \left[1 - \left(\frac{U}{U_e}\right)^2\right] + \frac{T_w - T_{ad}}{T_e} \left(1 - \frac{U}{U_e}\right)$$

and the perfect gas law. The turbulent recovery factor r, was taken equal to 0.88.

3.0 RESULTS AND DISCUSSION

Holographic interferometry data were obtained at five Mach numbers, M_∞ = 0.3, 0.5, 0.6, 0.65, and 0.7. At each Mach number a range of plenum blowing pressures were applied including the baseline no-blowing conditions. Also, data were obtained for two angles of attack, $\alpha = 0°$ and $-5°$. Because of the limitations of time, the holographic interferometry data obtained at $M_\infty = 0.3$ have not yet been reduced. As a result of a fault in the manufacture of the holographic plates, the interferograms are less than optimum. However, to our knowledge these data are the first interferograms of circulation control airfoil flows at transonic speeds. The results provide much needed flow visualization and quantitative information required in the understanding of the Coanda effect at transonic speeds.

The data shall be presented in the order of increasing Mach numbers. Figures 5a, b, c, d, and e are the interferograms for the $M_\infty = 0.5$, $\alpha = 0°$ case at blowing pressures of 0, 15, 20, 25, and 30 psi. Each fringe line is a constant density contour since the interferometer was aligned in the infinite fringe mode. It should be understood that the interferometry technique integrates the density field over the entire span of the airfoil. Three-dimensional effects at the sidewalls can introduce errors into the measurements. However, the three-dimensional effects are typically confined to the sidewall boundary layers. Because the beam passes normal to the boundary layer, the effects are, in most part, insignificant.

One indication of the two-dimensionality of the flow can be seen in figure 5a. Without blowing, a very well-defined vortex street was formed which appears as circular fringes in the wake. The boundary layers from the upper and lower surfaces detached from the airfoil at

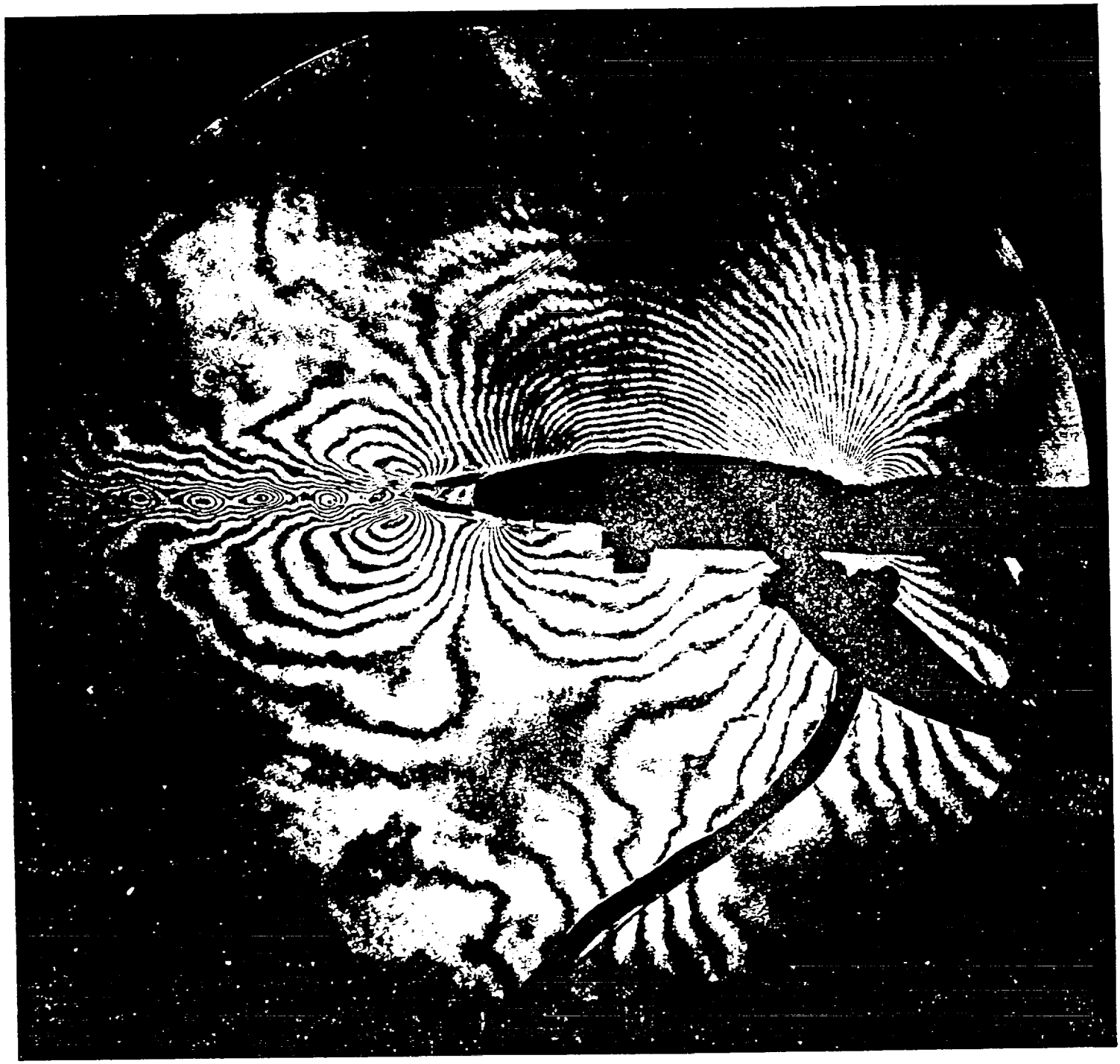

(a) P_{B1} = 0 psi

Figure 5.- Interferograms of the flow field at M_∞ = 0.5, α = 0°.

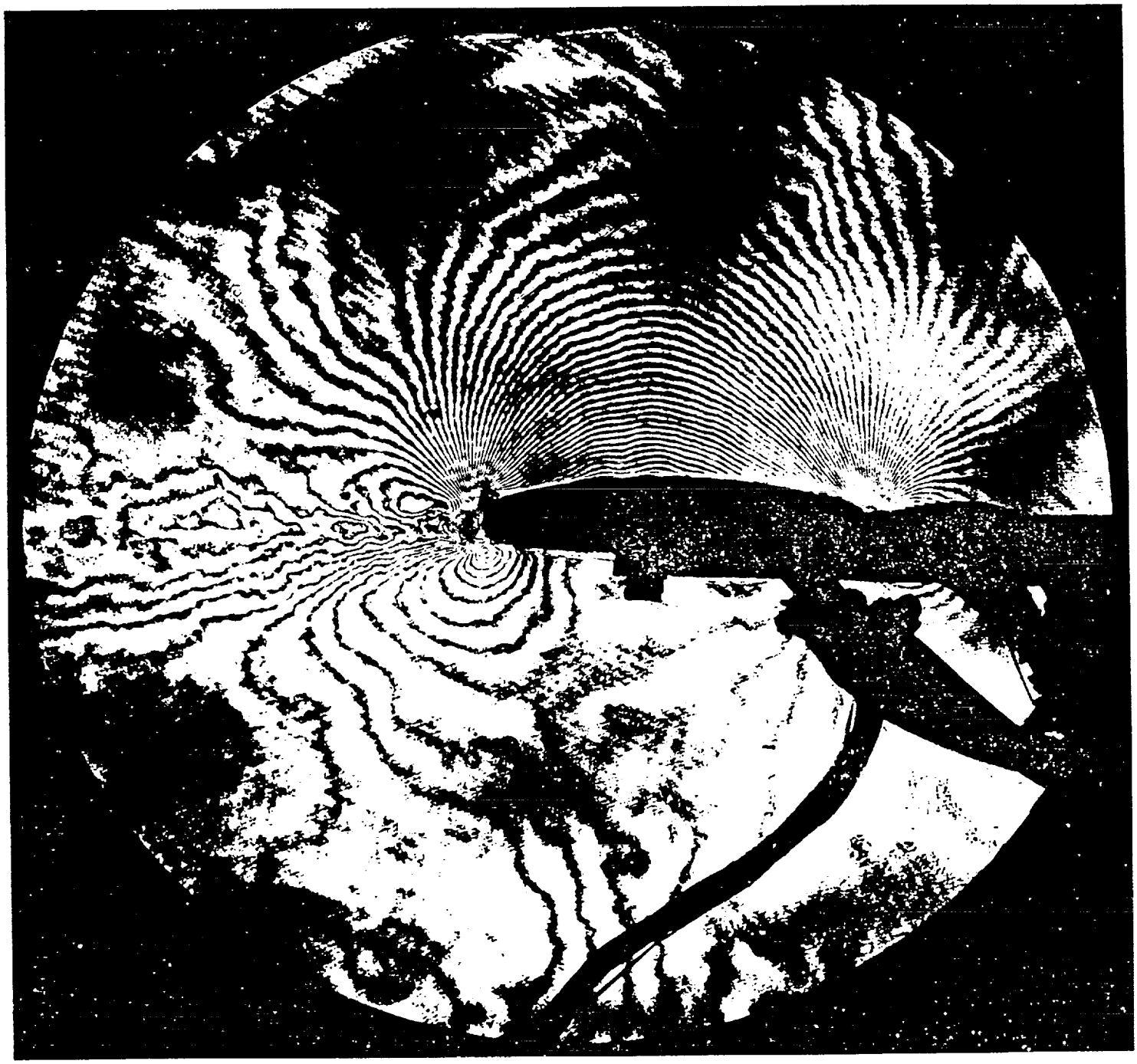

(b) P_{B1} = 15 psi

Figure 5.- Continued.

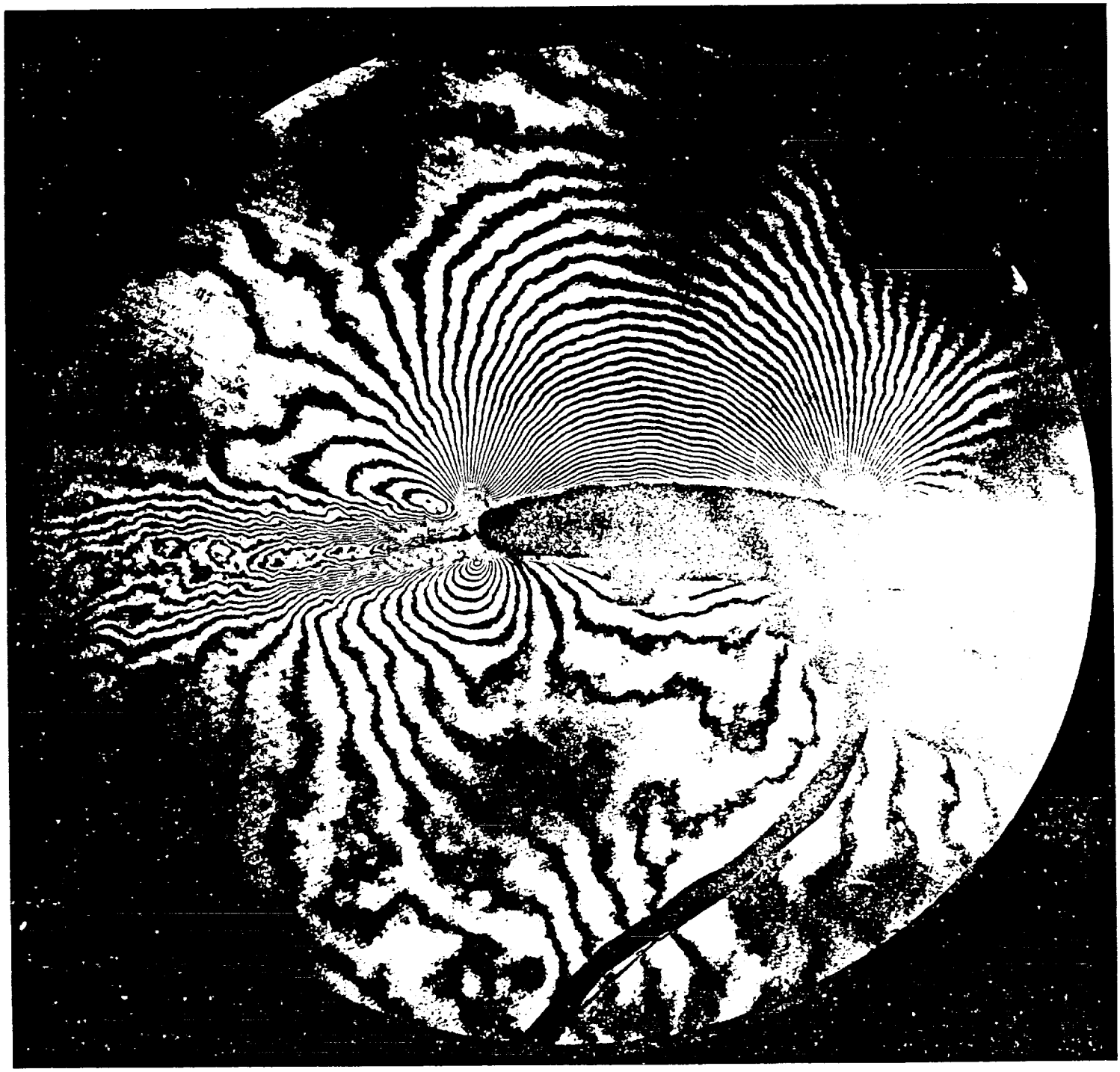

(c) P_{Bi} = 20 psi

Figure 5.- Continued.

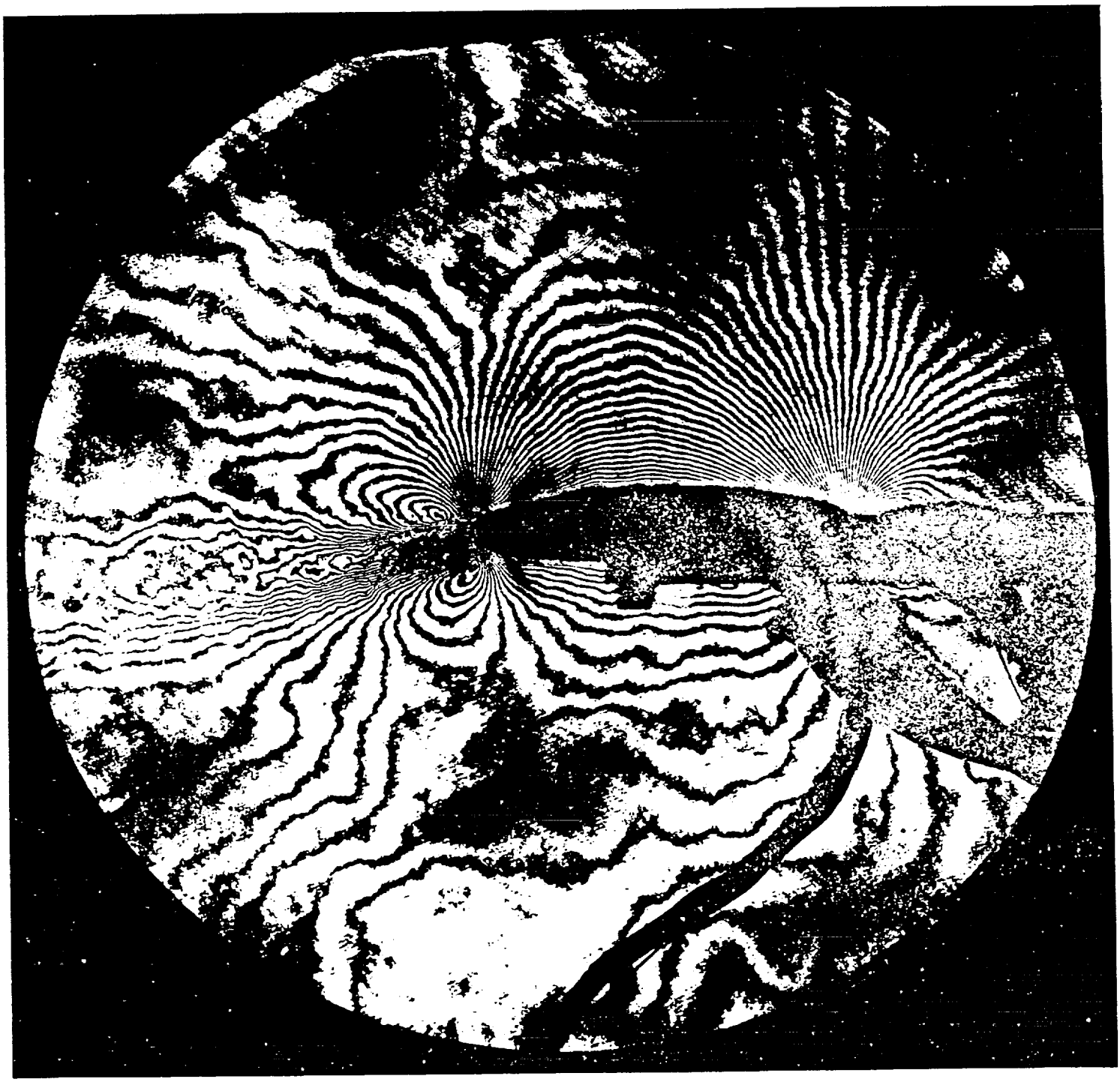

(d) P_{B1} = 25 psi

Figure 5.- Continued.

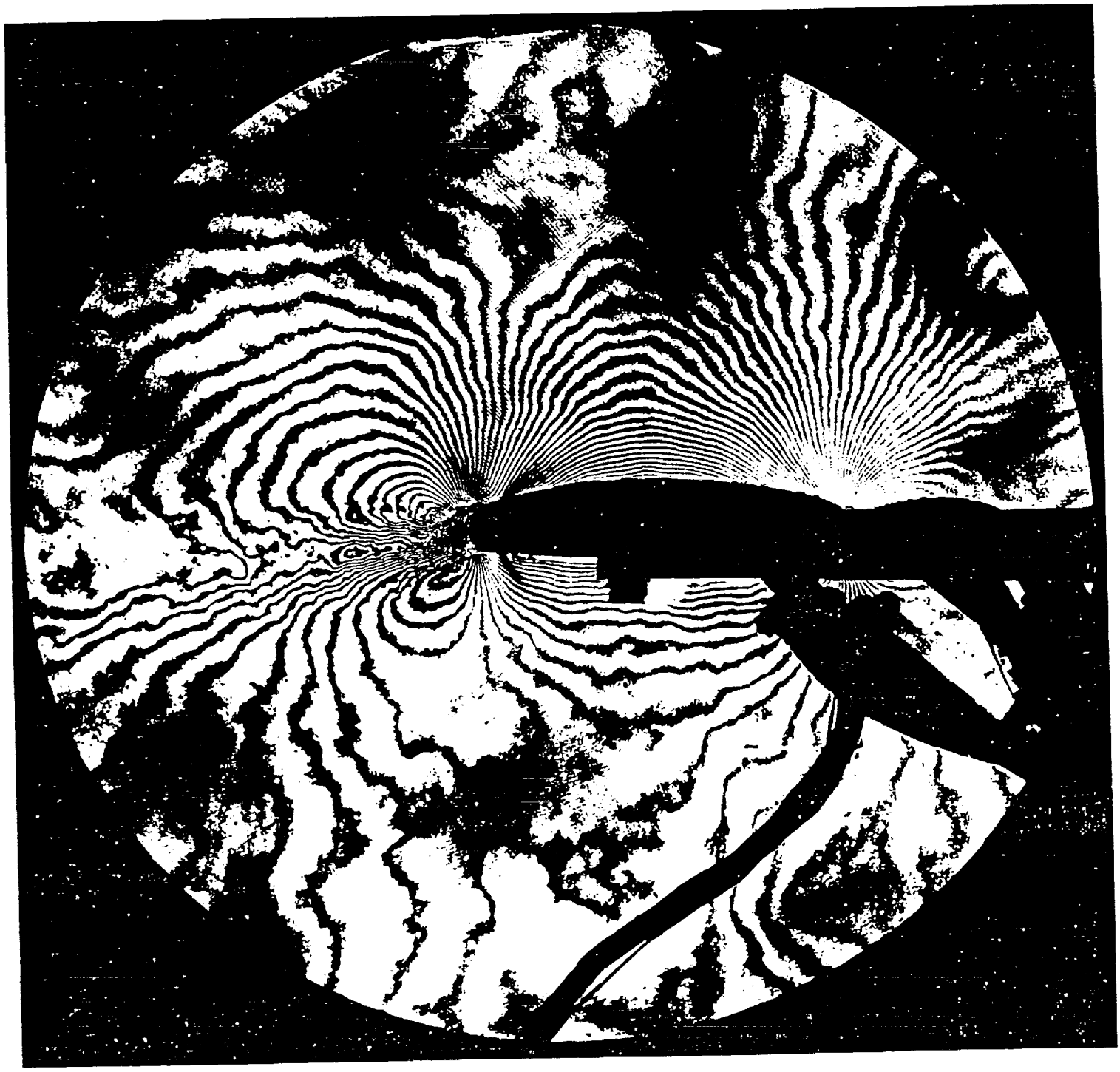

(e) P_{B1} = 30 psi

Figure 5.- Concluded.

tangency points approximately where the blunt trailing-edge curvature began. The viscous shear layers can then be observed to interact and roll up into two-dimensional vortices.

Other features to note as general characteristics of all of the zero blowing cases are the pressure gradients at the trailing edge and the peak pressure on the wake. The minimum pressure on the upper surface occurred at about 0.6 chord. Each fringe from there represents an increase in pressure (assuming isentropic flow). The pressure gradient moving toward the trailing edge was relatively steep to the point of boundary-layer detachment. An additional increase in the pressure gradient occurred leading to the interaction of the upper and lower shear layers. The two circular fringes above and below the wake are representative of local peak pressures.

Figure 5b shows the flow for a plenum blowing pressure of $P_B = 15$ psi. Whereas in the no-blowing case a rather large dead air region occurred in the near wake of the airfoil; with Coanda blowing, the flow remained attached at the base of the model. The dark region on the upper surface immediately downstream of the blowing slot was due to the large change in the pressure (density) that caused a deflection of the light rays from this region. Fringes approaching the jet are approximately tangent to the model in this case indicating change that was produced in the inviscid flow by the reduced pressure gradient at the trailing edge. A very strong streamwise pressure gradient was present immediately downstream of the trailing edge of the model. The rear stagnation point indicated by the sketched fringe pattern was moved around the trailing edge. The peak pressure indicated by the center of the concentric fringes was also moved to a point beneath the trailing edge of the airfoil. The net effect of the movement of the rear stagnation and the peak pressure points

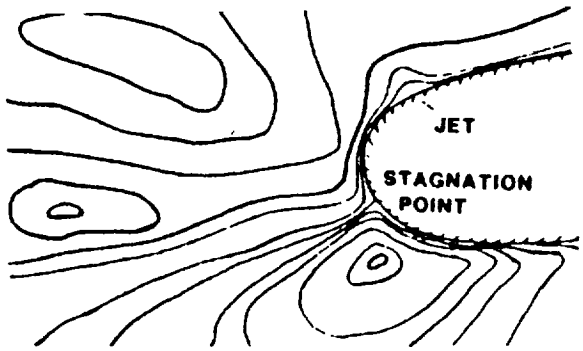

was to increase the effective camber of the airfoil, and hence, the circulation. Flow on the lower surface of the airfoil was relatively uniform as indicated by the few broad fringes there. The wake was deflected downward by the circulation and spread rapidly as a result of the vertical momentum introduced by the jet.

Increasing the blowing pressure to $P_{B1} = 25$ (fig. 5d), did not produce a noticeable effect on the flow at the upper surface. However, the pressure on the lower surface of the airfoil was increased followed by an increased pressure gradient to the rear peak pressure. A further increase in the jet plenum pressure to $P_{B1} = 30$ (fig. 5e), resulted in the partial separation of the jet as indicated by the following sketch of the fringe pattern:

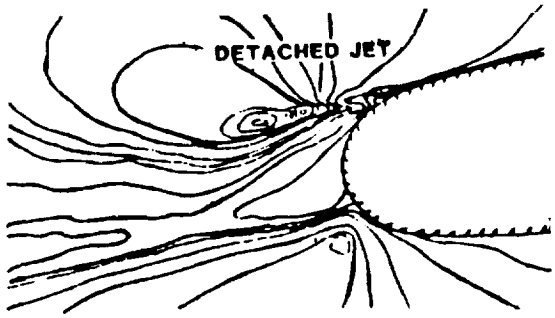

Although the jet was partially separated, there appeared to be a component that remained attached to the wall and continued to turn about the trailing edge to produce an overall flow field similar to the previous blowing level. This can be seen more clearly on the enlargement of the trailing edge views of the flows.

Figures 6a, b, c, d, and e are interferograms obtained at $M_\infty = 0.5$ and $\alpha = -5°$ for comparison to the $\alpha = 0°$ case. A major difference was the pressure distribution on the lower surface. The presence of fringes normal to the lower surface is indicative of an increased pressure gradient toward the trailing edge of the airfoil. As may have been expected, the minimum pressure on the upper surface moved downstream. Careful comparison of the $P_B = 15$ psia cases, for example, revealed some other differences in the two cases. The wake in the $\alpha = -5°$ remained more organized whereas the $\alpha = 0°$ wake spread rapidly. Also, because of the reduced momentum of the flow on the lower surface of the $\alpha = -5°$ case, the disruption of the Coanda jet was not as pronounced. This phenomena may explain the behavior of the C_ℓ versus blowing coefficient, C_μ (Wood and Conlon[6]), which showed a sharp drop in C_ℓ as the blowing was increased beyond a critical point. This sharp drop in the lift coefficient was diminished at negative angle of attack.

A plot of C_ℓ versus C_μ obtained by Wood and Conlon is shown in figure 7. The drop in the C_ℓ curve may have resulted from a partial separation of the jet which may be expected to increase rapidly as the angular momentum of the jet exceeded the static pressure force holding it to the wall. When the jet separated, the momentum flux in the freestream direction increased and was less effect in entraining the flow on the upper surface and thus impeding the flow on the lower surface. The high velocity of the separated jet produced a reduced static pressure and fluid entrainment which then caused the rear stagnation point to move upward. As the momentum of the jet is increased, the jet may be expected to turn further toward the freestream direction and entrain flow from the lower surface as well.

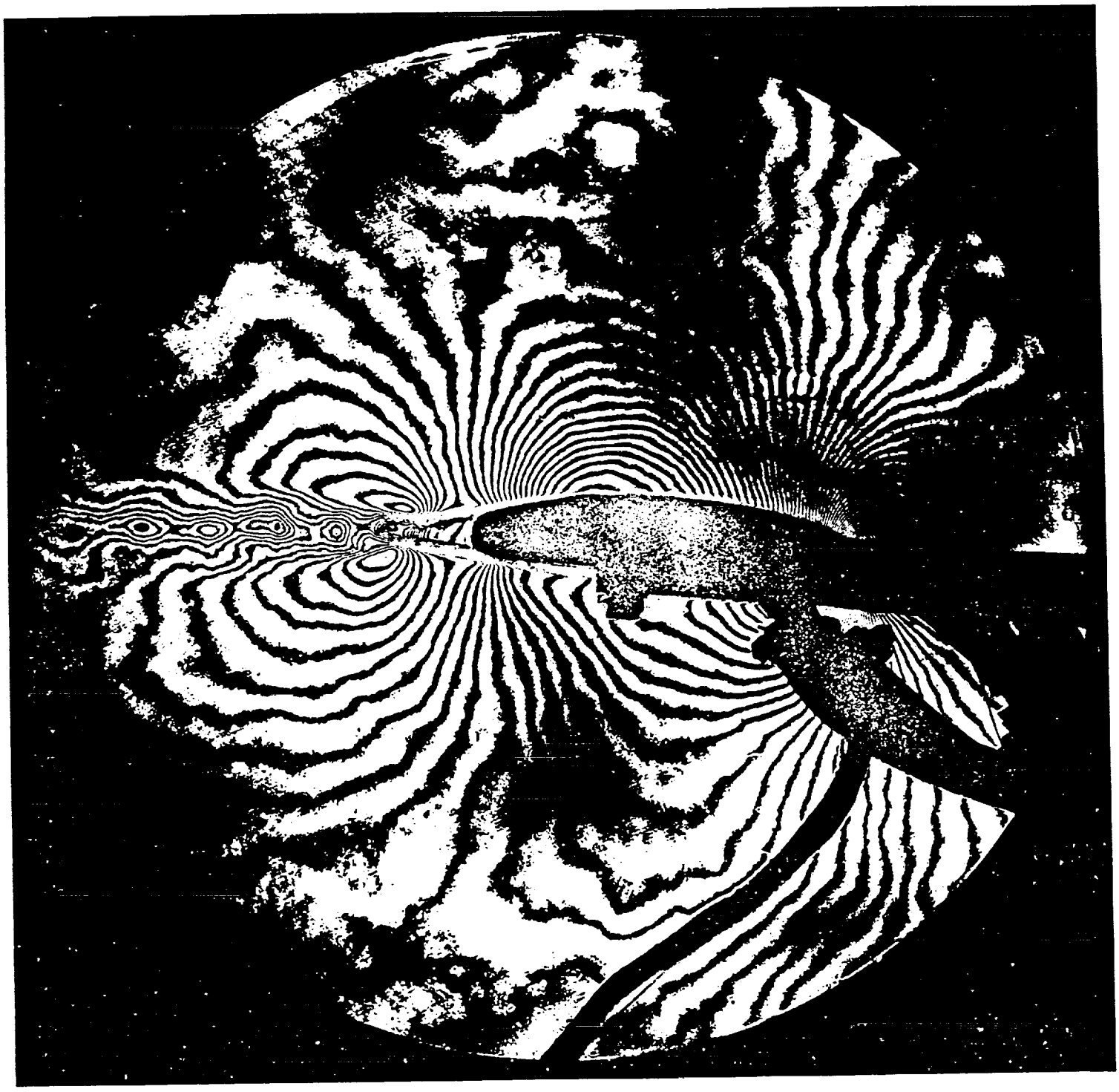

(a) P_{B1} = 0 psi

Figure 6.- Interferograms of the flow field at $M_\infty = 0.5$, $\alpha = -5°$.

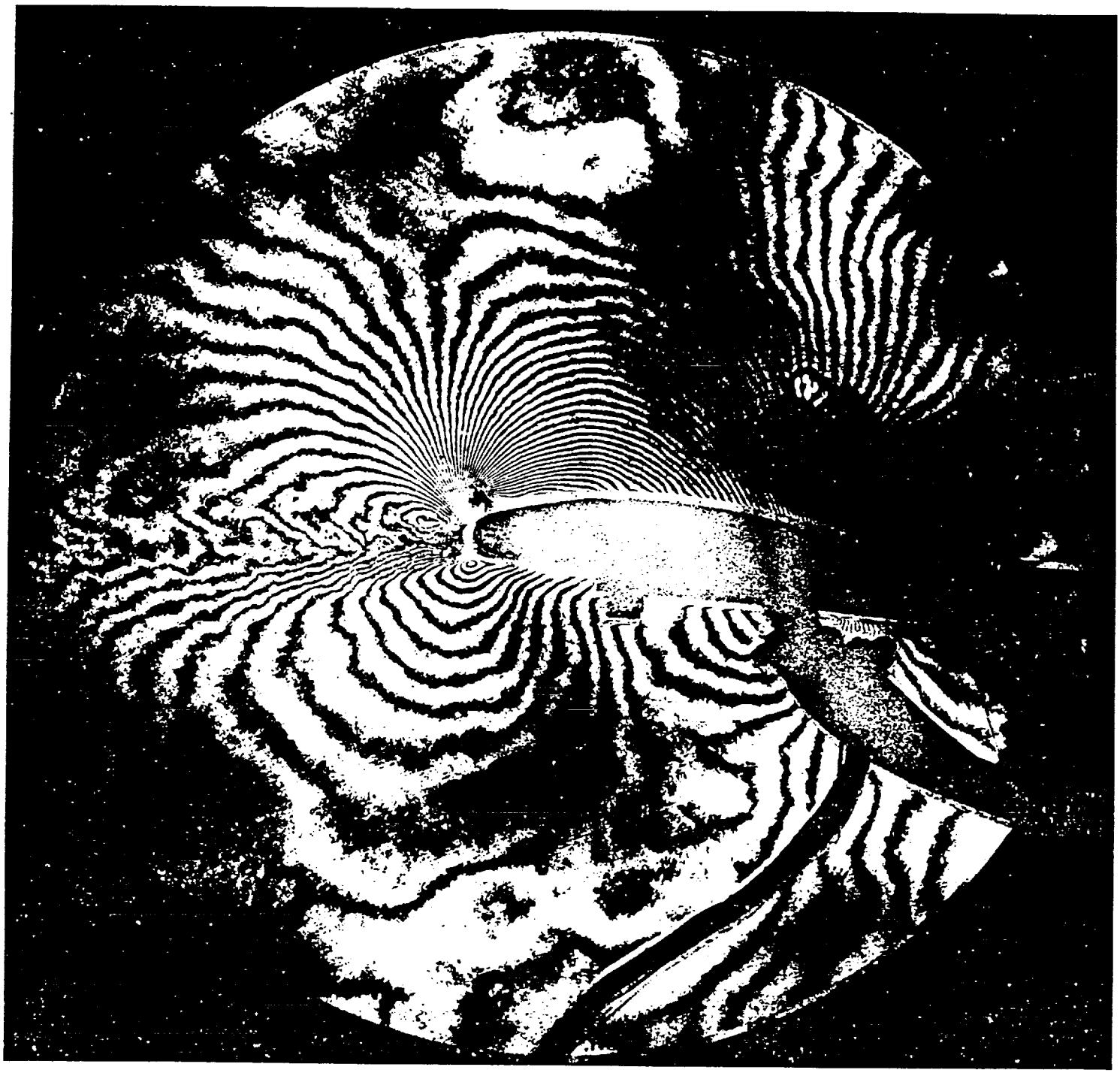

(b) P_{B1} = 10 psi

Figure 6.- Continued.

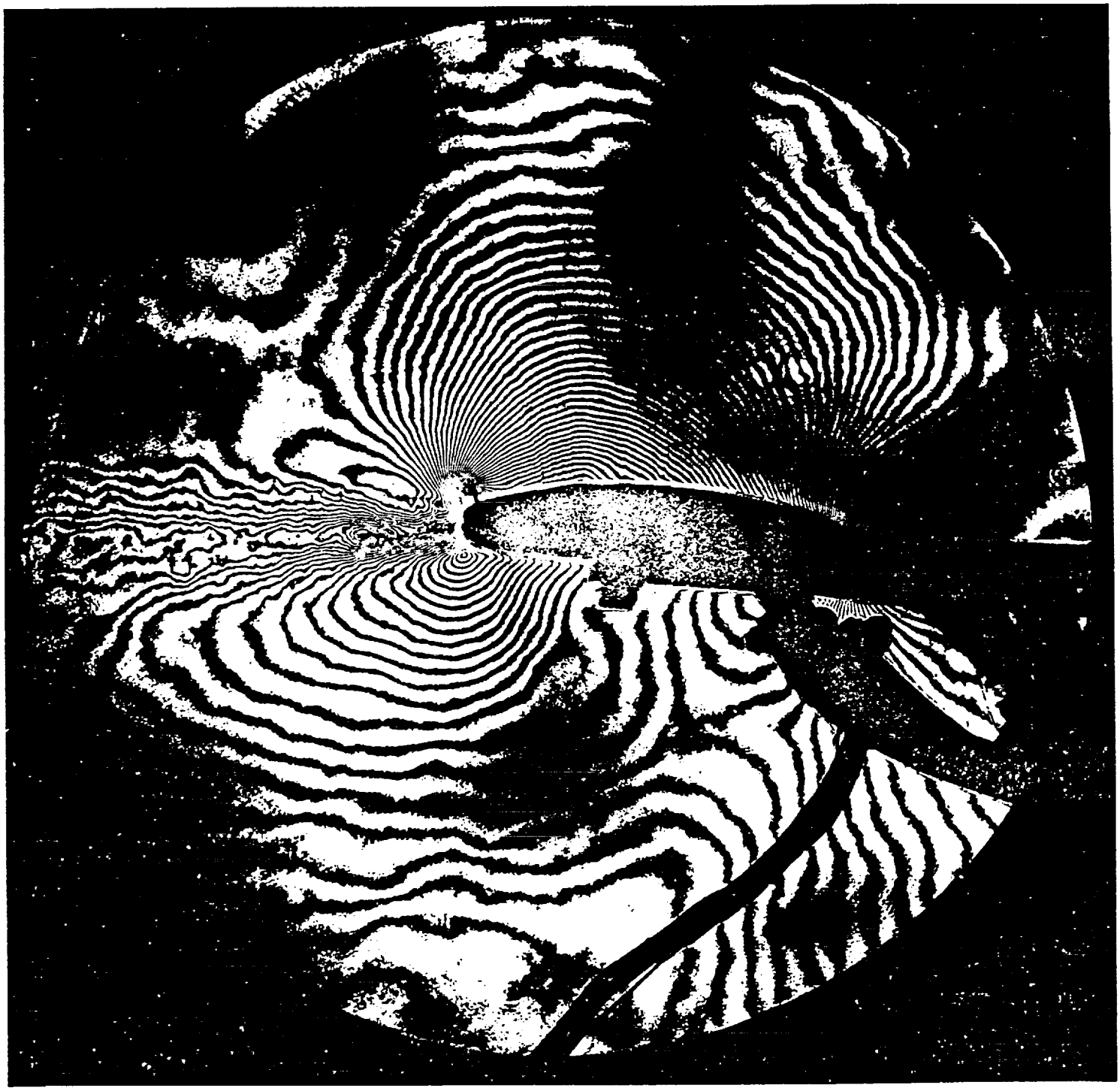

(c) P_{B1} = 15 psi

Figure 6.- Continued.

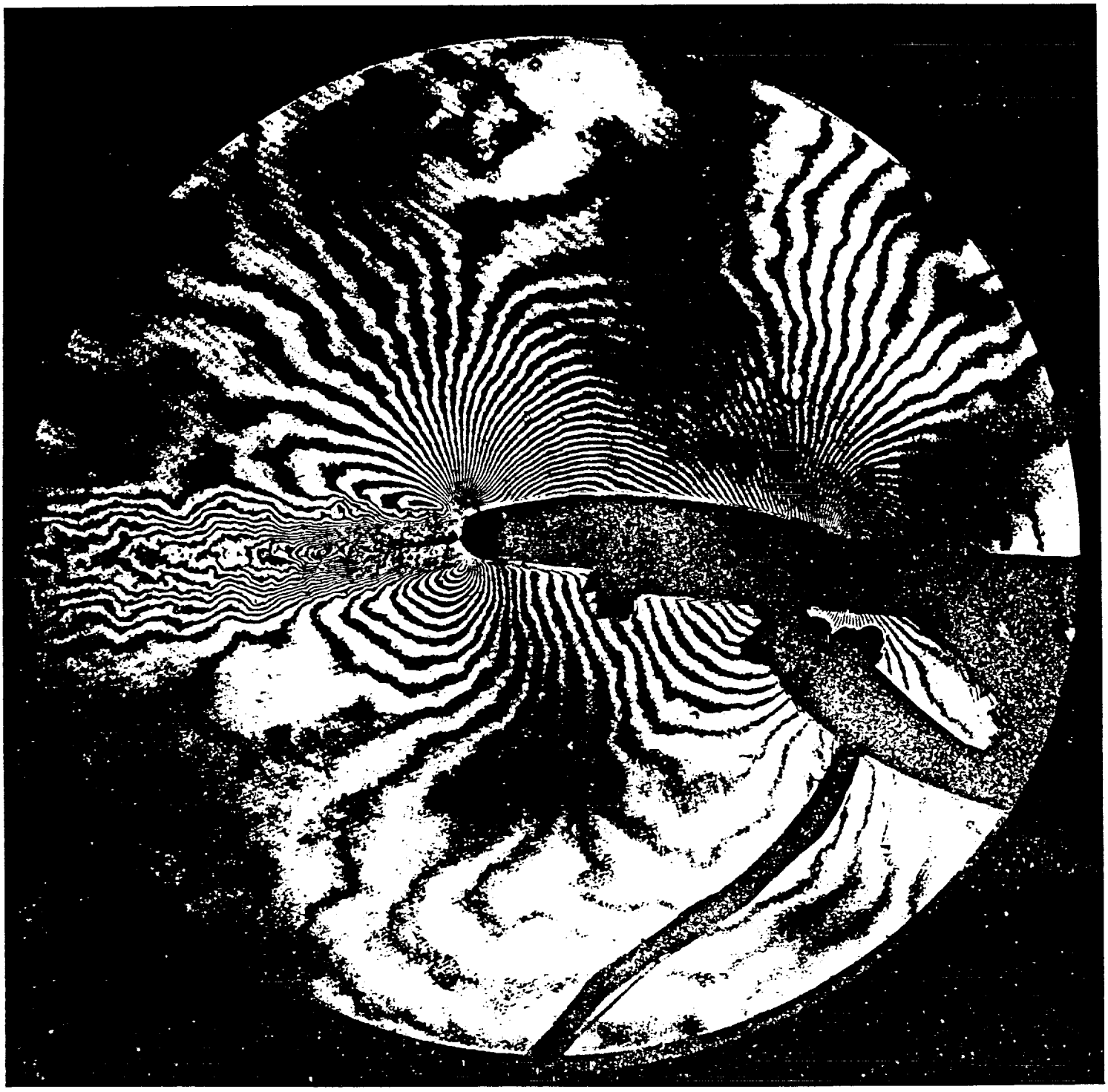

(d) P_{B1} = 20 psi

Figure 6.- Continued.

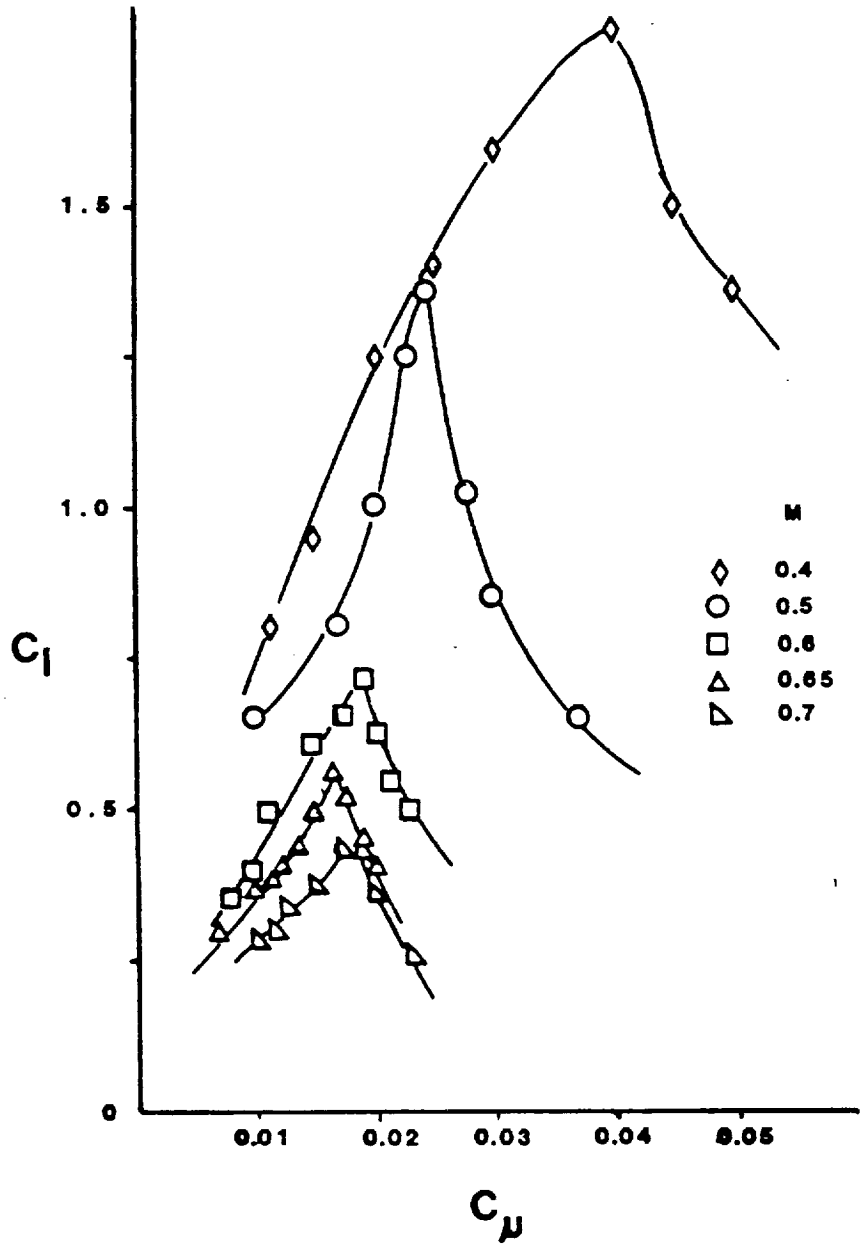

Figure 7.- Plot of lift coefficient with blowing at a range of freestream Mach numbers.

A schematic of the attached and the separated jet flows are shown in figures 8a and b. Note that in the fully attached case (fig. 8a), the jet encounters the flow on the lower surface at approximately a normal angle. When jet separation occurs (e.g., fig. 5e), the jet is approximately parallel to the freestream direction.

At higher Mach numbers, greater blowing pressures were required to affect the flow. For example, at $M_\infty = 0.6$, figures 9a, b, c, d, and e, a blowing pressure $P_B = 17$ was required to produce significant flow entrainment at the trailing edge. It is interesting to note that a small change in blowing pressure from $P_B = 15$ to $P_B = 17$ (figs. 9d and e) caused the flow to remain attached moving the stagnation point around the trailing edge of the airfoil. At this Mach number, the flow on the upper surface was approaching critical conditions as seen by the compression waves on figure 9e.

When the Mach number was increased to $M_\infty = 0.65$ (figs. 10a, b, c, d, and e), the compression waves on the upper surface could be observed for all blowing conditions tested. Unlike at the lower Mach numbers, the boundary layers from the upper and lower surfaces separated even with blowing pressures as high as 15 psia. However, the Coanda jet is visible as it remained attached around the trailing edge. Only after the blowing was increased to $P_B = 20$ psia did the flow remain attached. But at this blowing condition there was evidence of incipient jet separation. In figure 9e the jet was partially separated although the inner part of the jet appeared to remain attached to the model surface. There was also evidence of a high level of turbulence in the base-flow region immediately downstream of the model. Momentum introduced by the jet was still effective in closing the wake well upstream of the no-blowing case.

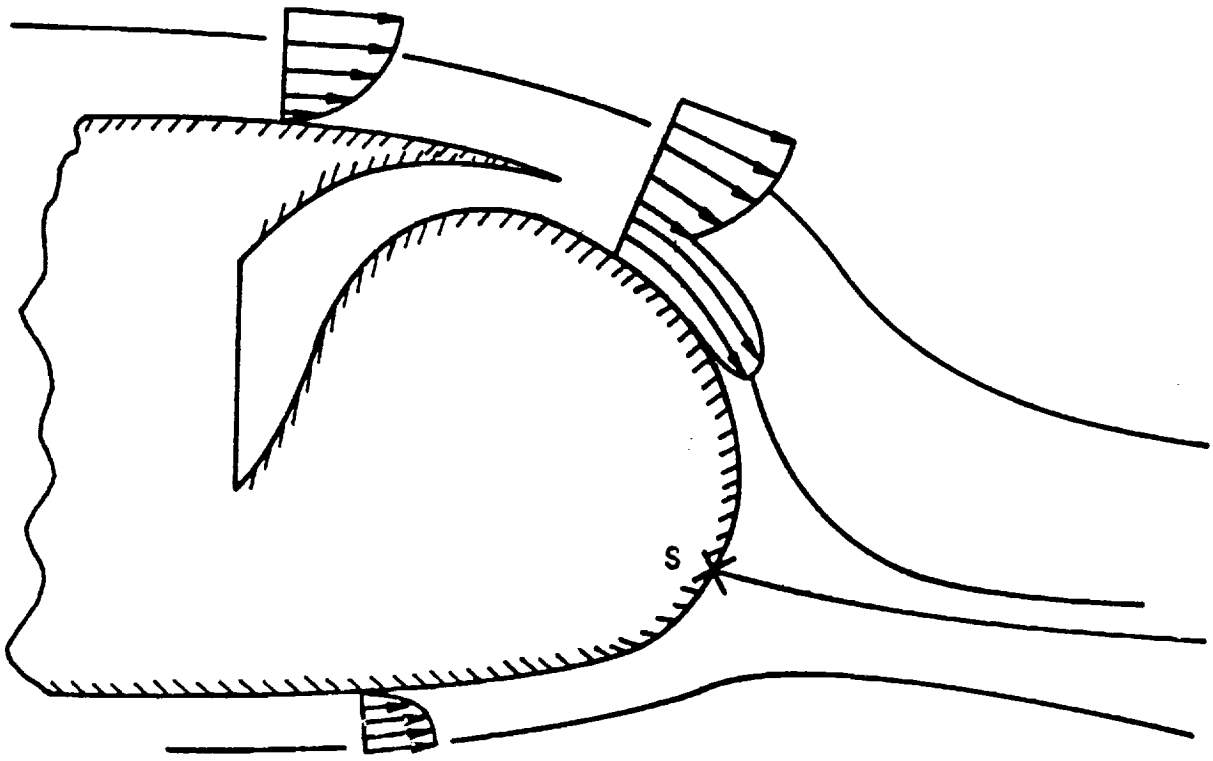

(a) Attached jet.

Figure 8.- Schematic of the trailing-edge flow field.

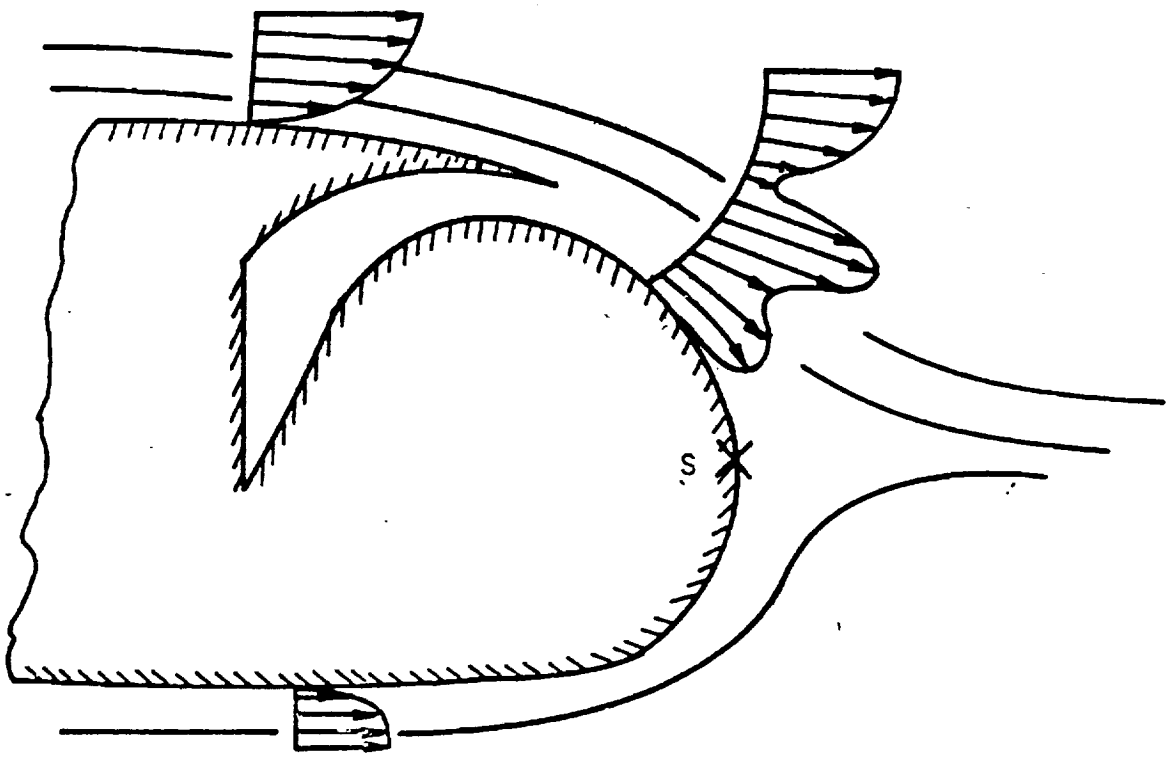

(b) Detached jet.

Figure 8.- Concluded.

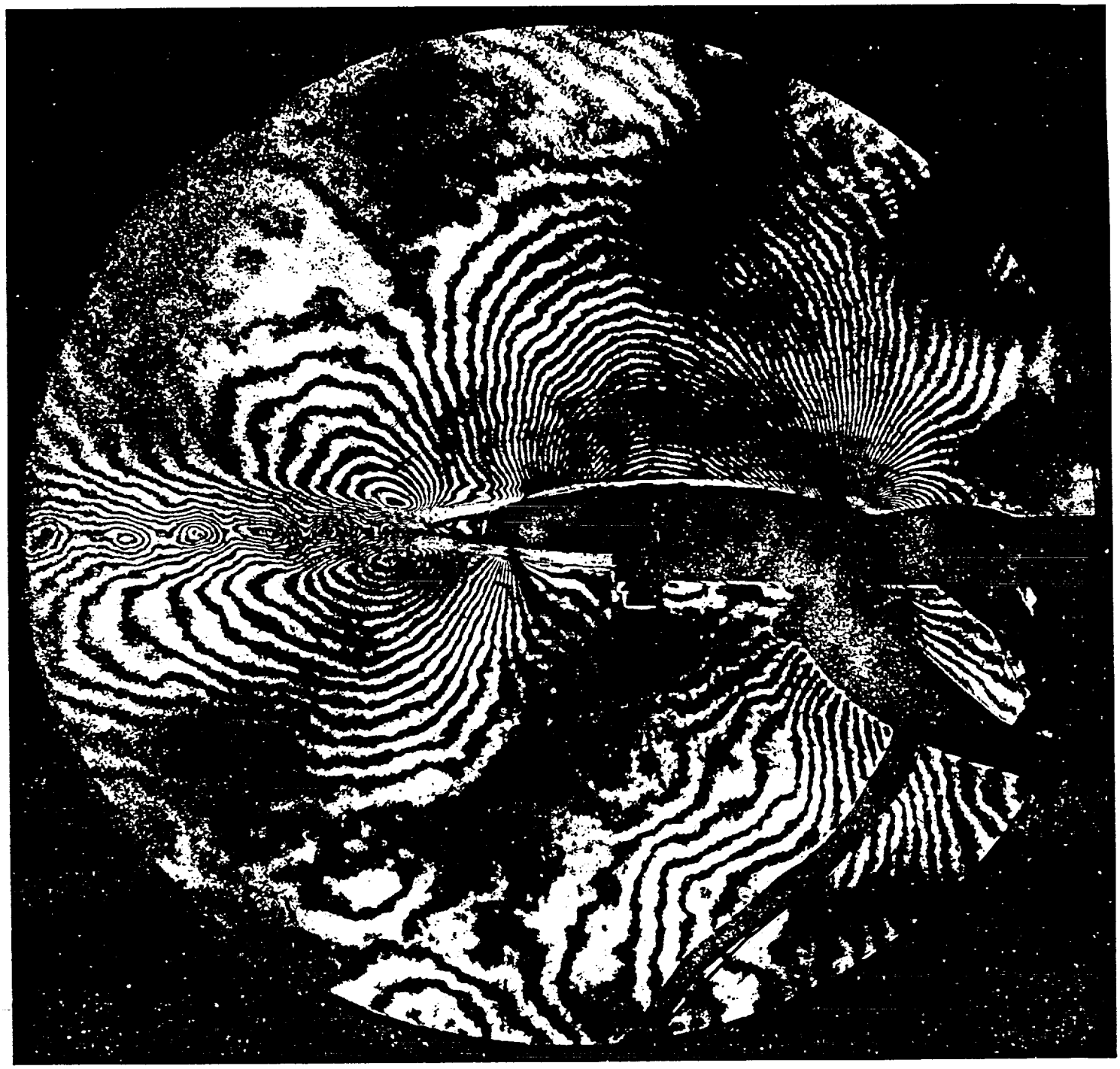

(a) P_{B1} = 0 psi

Figure 9.- Interferograms of the flow field at M_∞ = 0.6, α = 0.

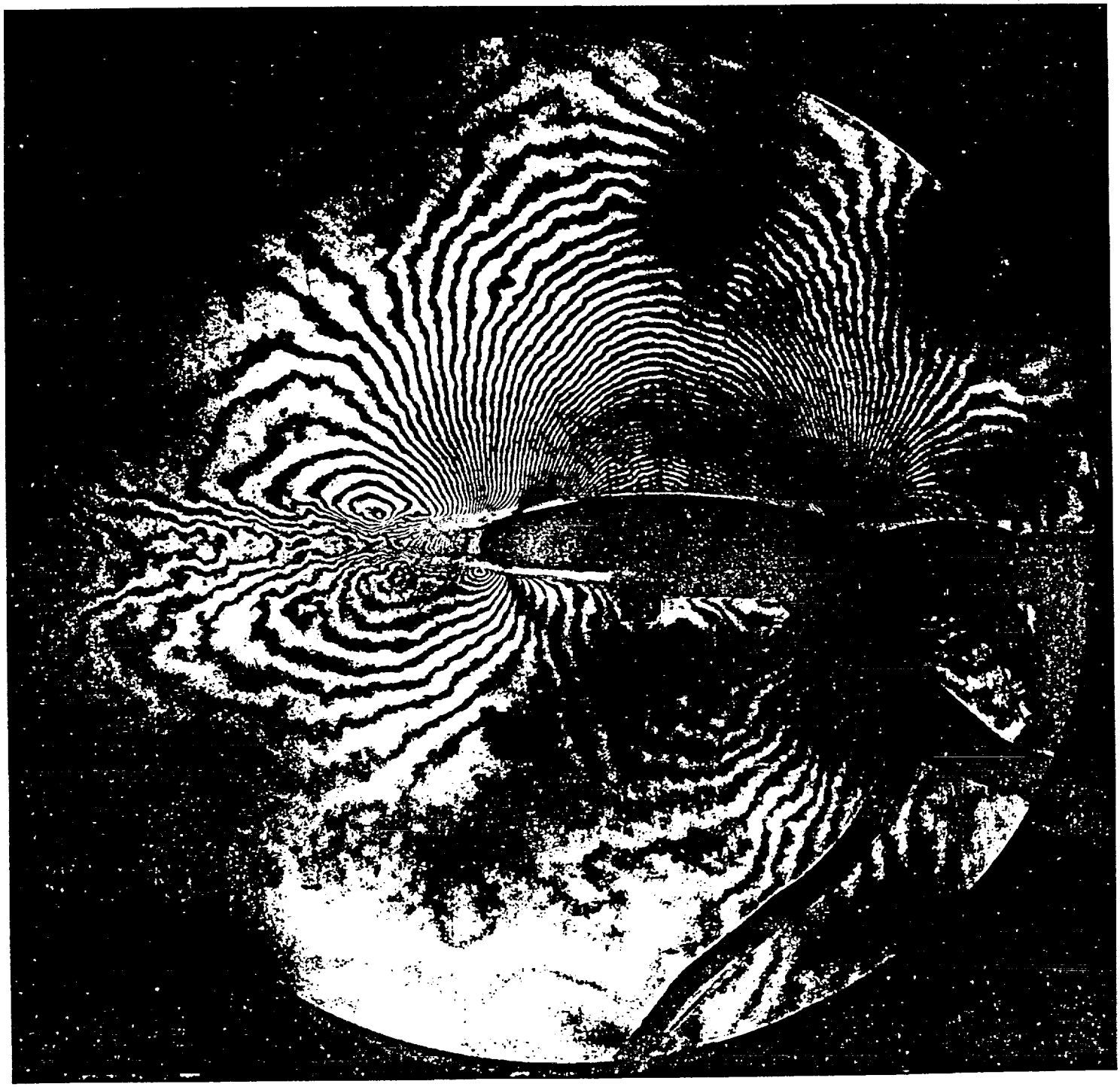

(b) P_{B1} = 10 psi

Figure 9.- Continued.

(c) P_{B1} = 12 psi

Figure 9.- Continued.

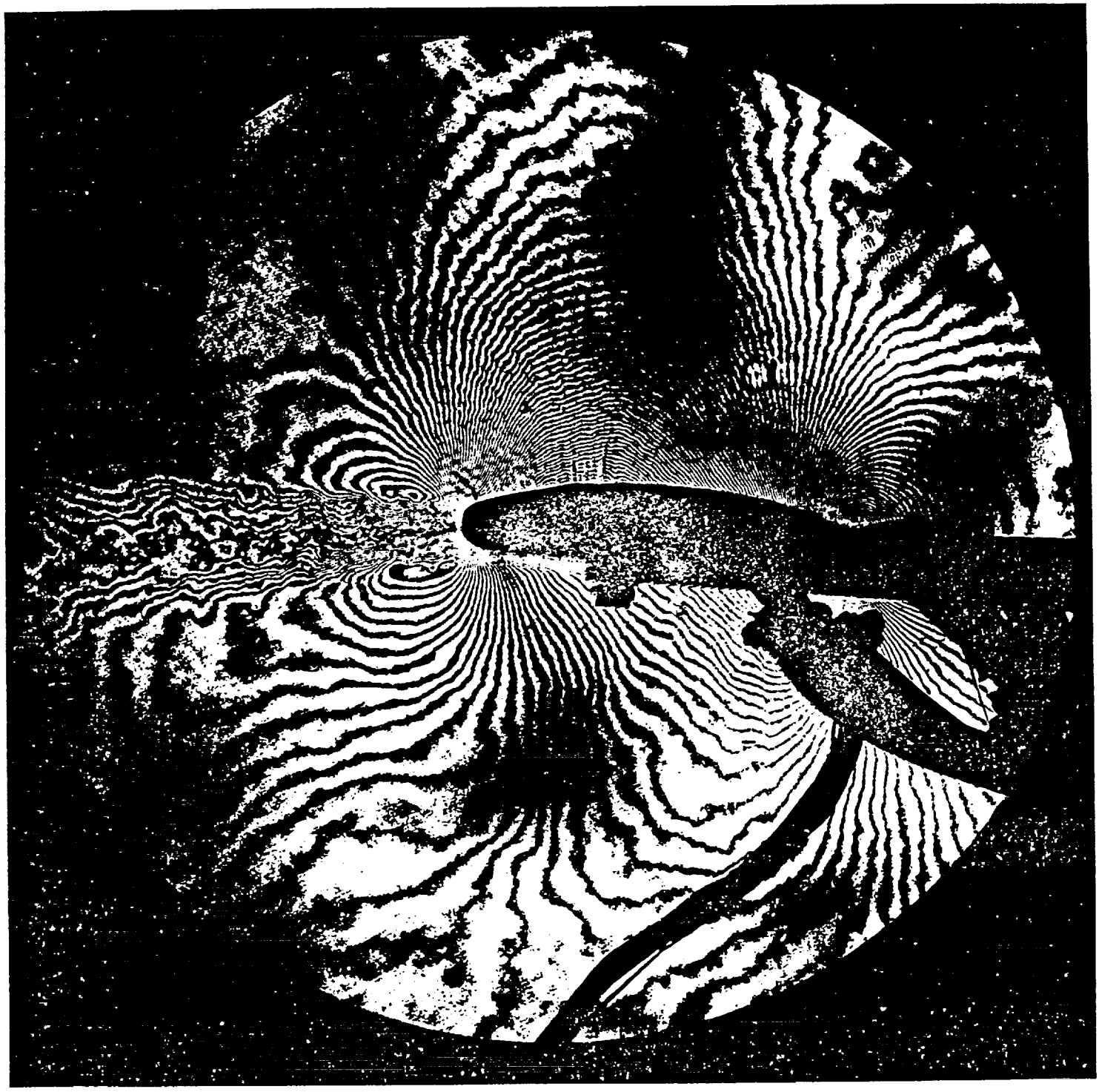

(d) P_{B1} = 15 psi

Figure 9.- Continued.

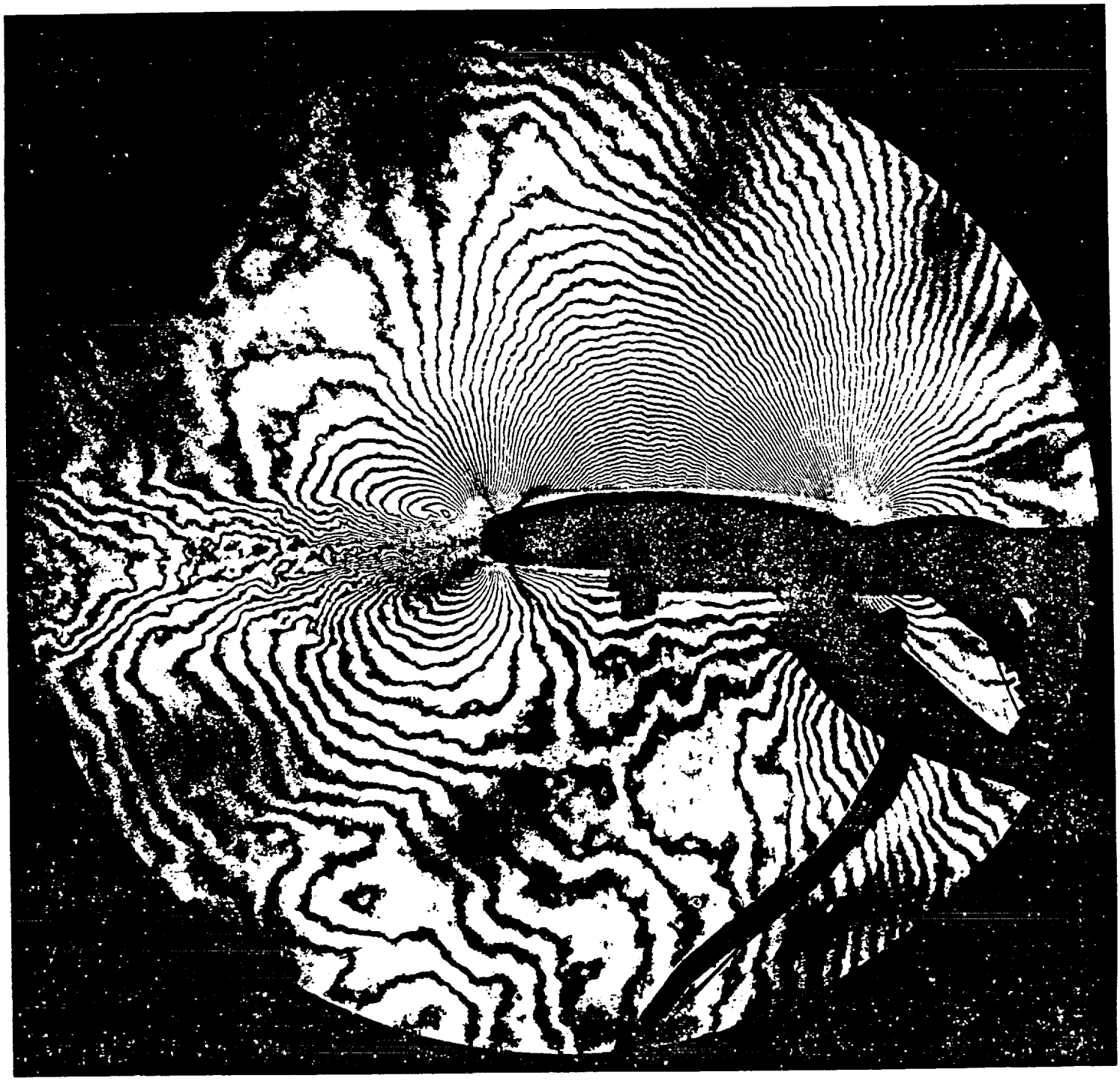

(e) P_{B1} = 17 psi

Figure 9.- Concluded.

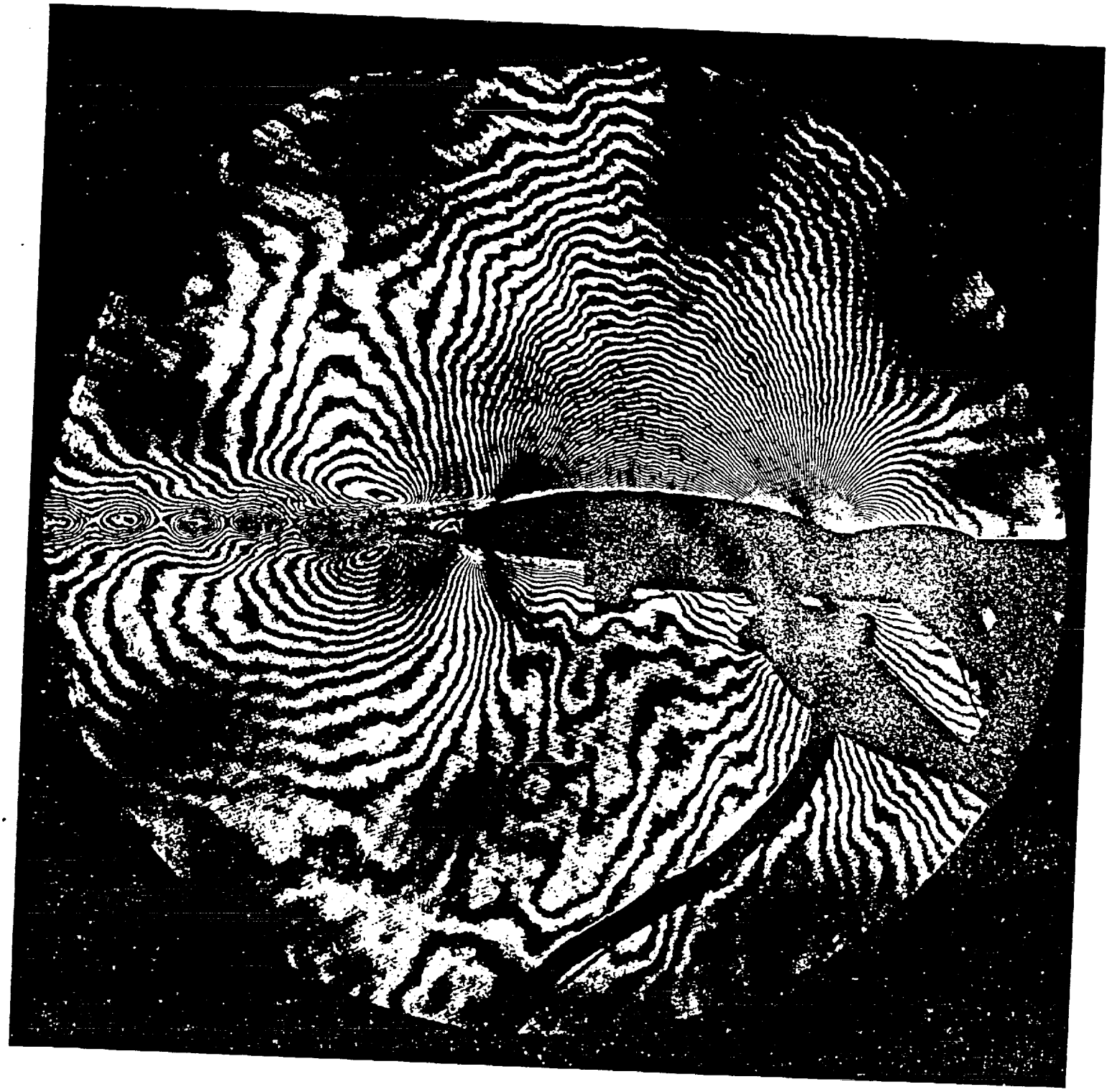

(a) P_{B1} = 0 psi

Figure 10.- Interferograms of the flow field at M_∞ = 0.65.

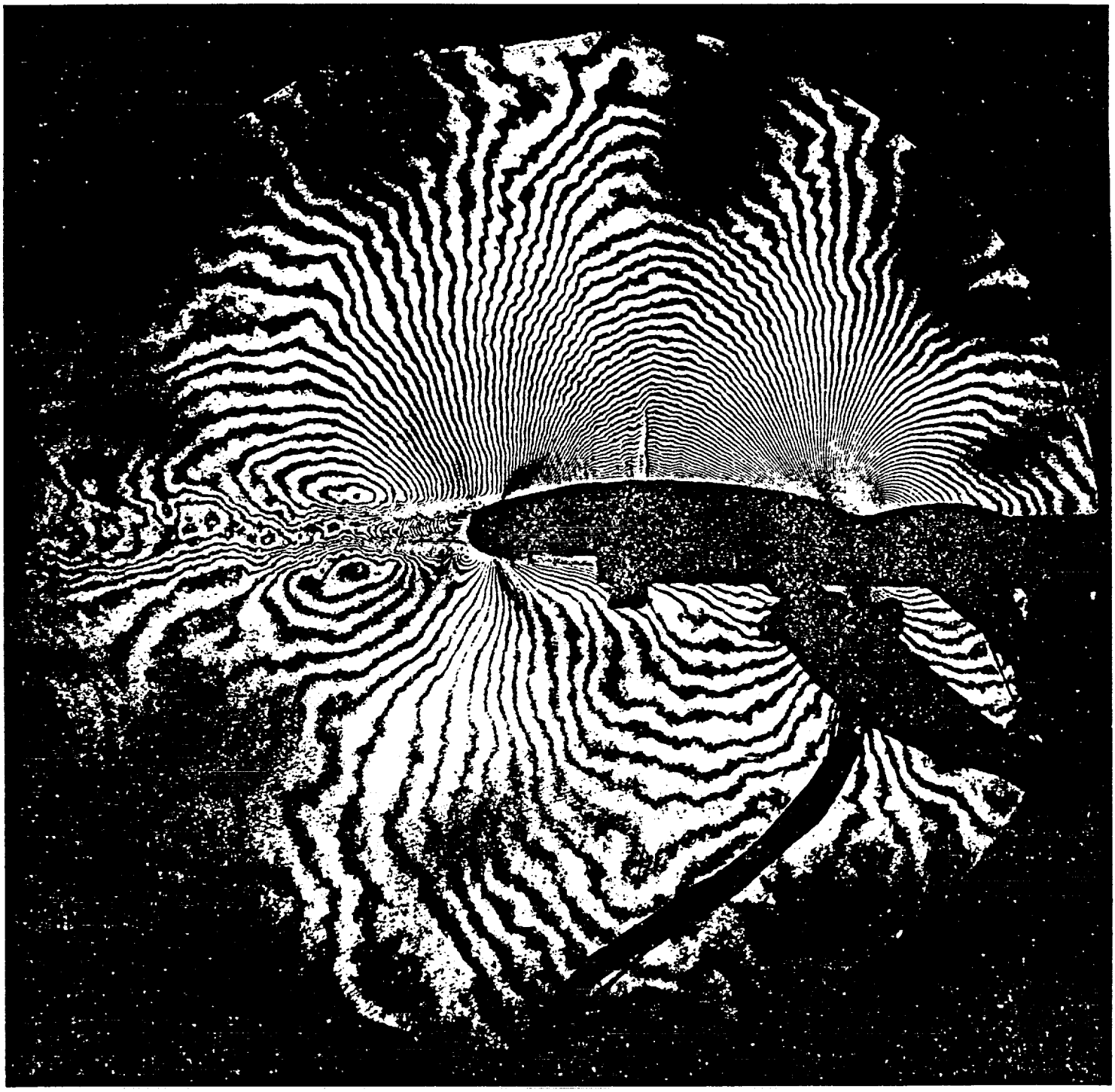

(b) P_{B1} = 10 psi

Figure 10.- Continued.

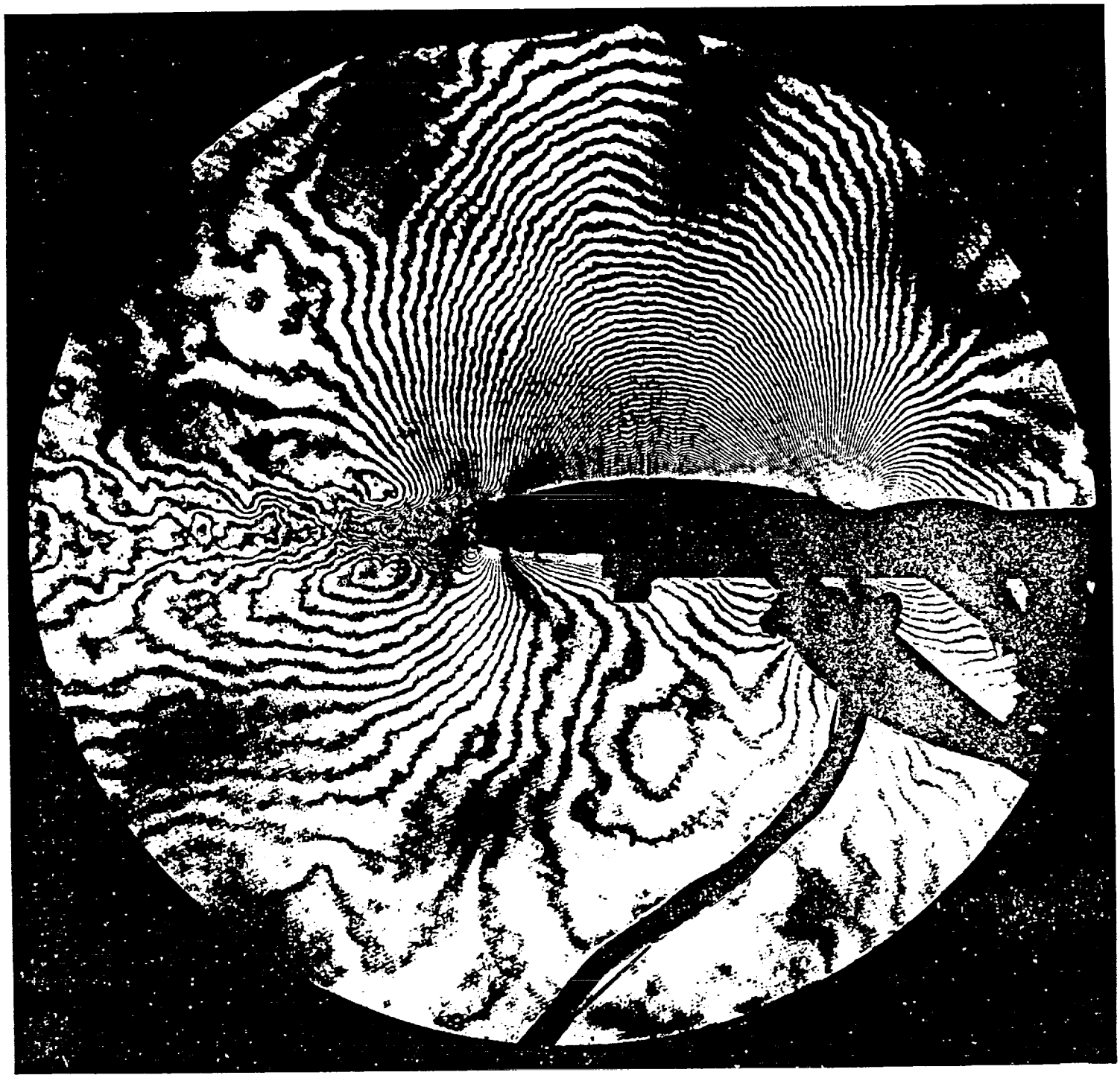

(c) P_{B1} = 15 psi

Figure 10.- Continued.

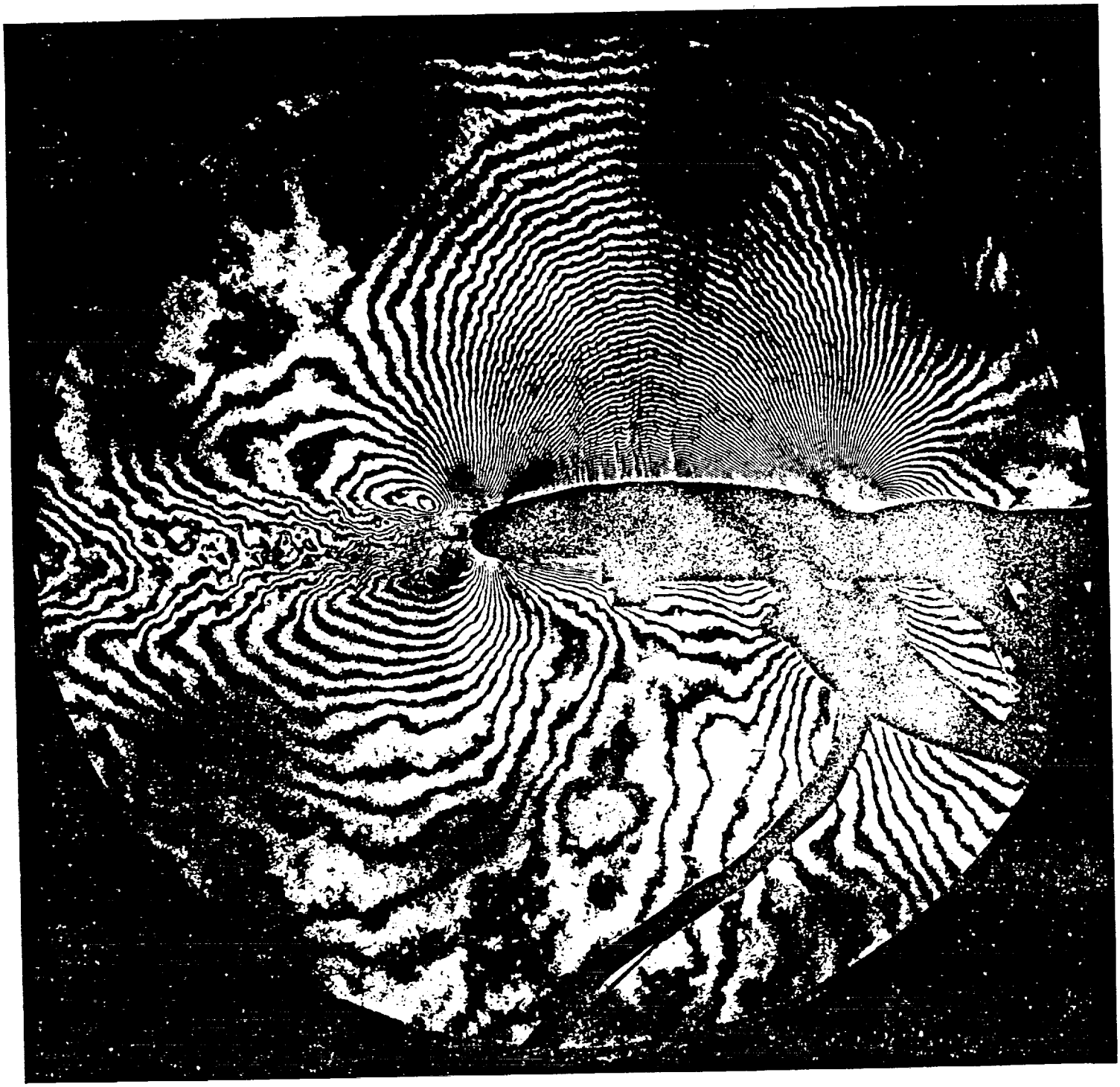

(d) P_{B1} = 20 psi

Figure 10.- Continued.

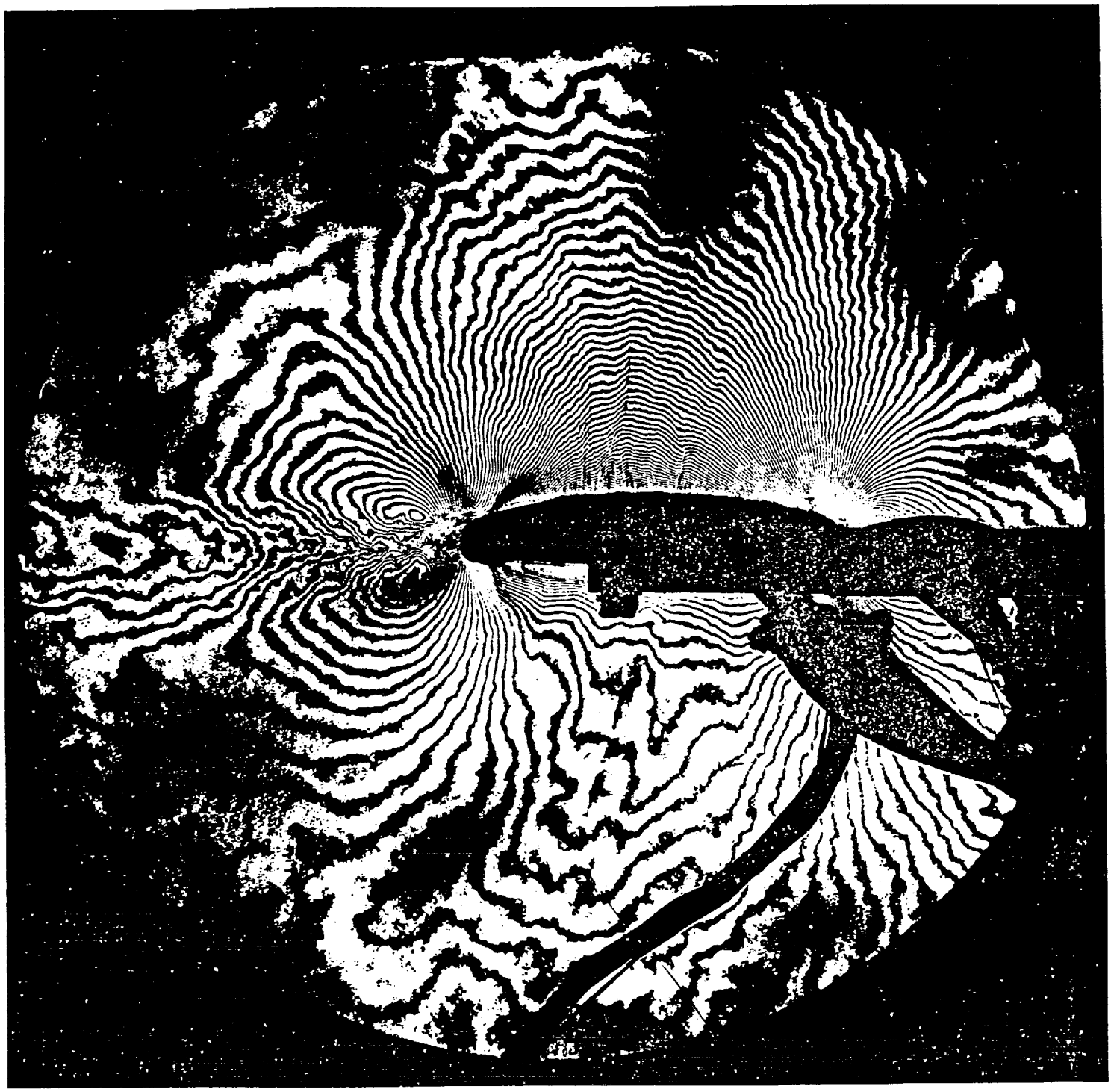

(e) P_{B1} = 30 psi

Figure 10.- Concluded.

At $M_\infty = 0.7$ (figs. 11a, b, and c), weak shock waves form at all blowing conditions. The increase in shock strength with increased blowing was due to the improved circulation decreasing the pressure in the aft region of the airfoil. Note that the increasing shock strength caused a definite thickening of the boundary layer which reduced the efficacy of the jet. Careful inspection of the enlarged view of the trailing edge reveals that the jet was clearly attached and interacted with the flow at the lower surface of the airfoil as in the lower Mach number cases. However, the flow entrainment did not occur and the inviscid flow outside the wake remained similar to the no-blowing case. A peak pressure region did occur at the trailing edge on the lower surface but this was a weak modification to the inviscid flow there. In both of the blowing cases shown, the Coanda jet remained attached to the rear stagnation point which did not appear to be as far around the airfoil trailing edge at the higher blowing pressure.

Some representative quantitative results were obtained from the interferograms to demonstrate the full potential of the technique. Also, pressures beyond the airfoil trailing edge could be obtained. In the neighborhood of the jet, the pressure at the edge of the boundary layer was expected to be significantly different from that on the surface. Comparisons of the measured surface pressure and the results from the interferograms was very reassuring especially when there was concern with the relative two-dimensionality of the flow.

Figures 12a and b show comparisons of the surface pressures obtained from the holographic interferometer and the surface pressure taps obtained at $M_\infty = 0.5$ and blowing pressures of $P_{B1} = 20$ and 30 psig. Note that the agreement was good except at the leading and trailing edges.

one page.

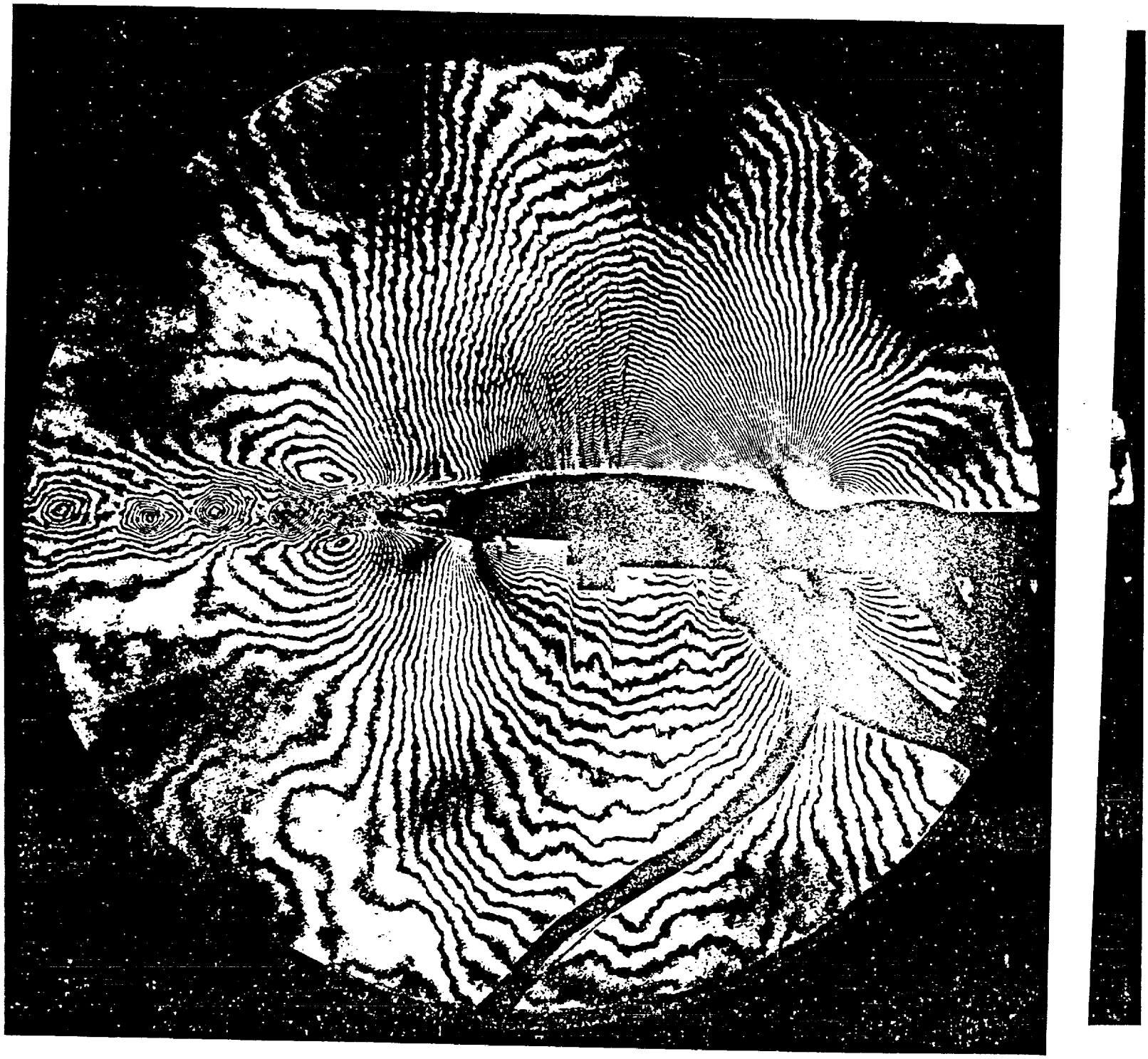

(a) P_{B1} = 0 psi

Figure 11.- Interferograms of the flow field at M_∞ = 0.7.

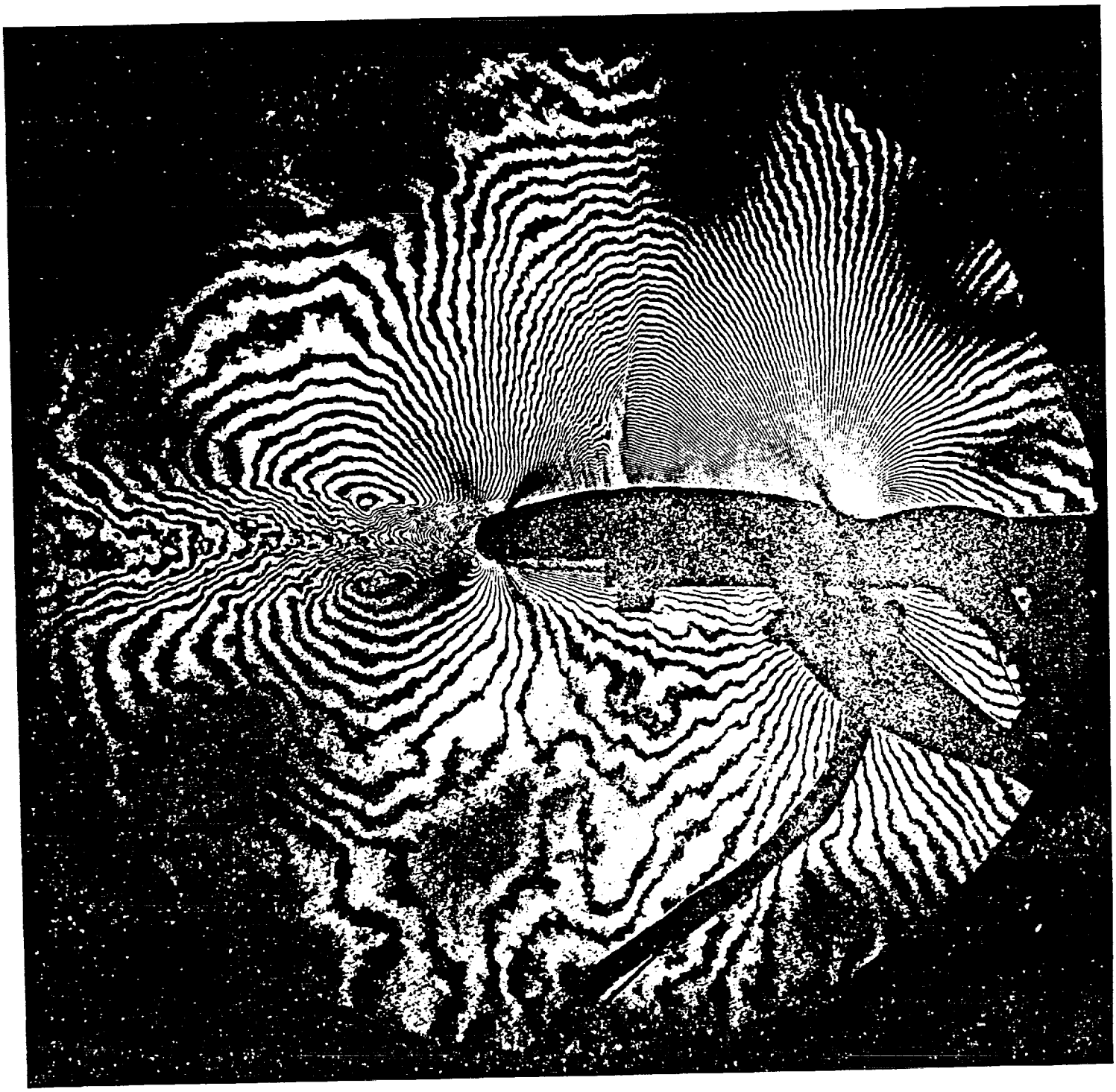

(c) P_{B1} = 20 psi

Figure 11.- Concluded.

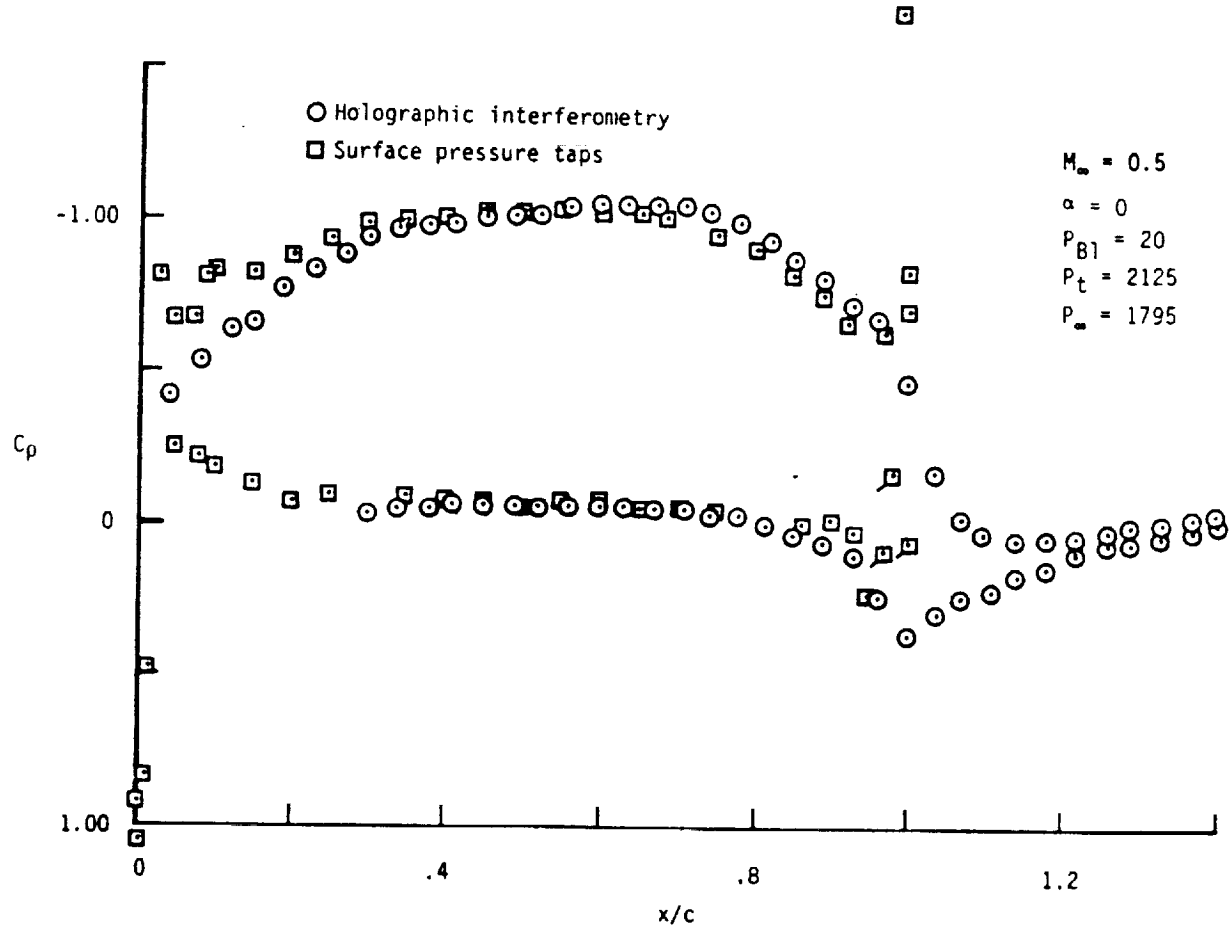

(a) P_{B1} = 20 psi

Figure 12.- Comparisons of the measured surface pressures at M_∞ = 0.5.

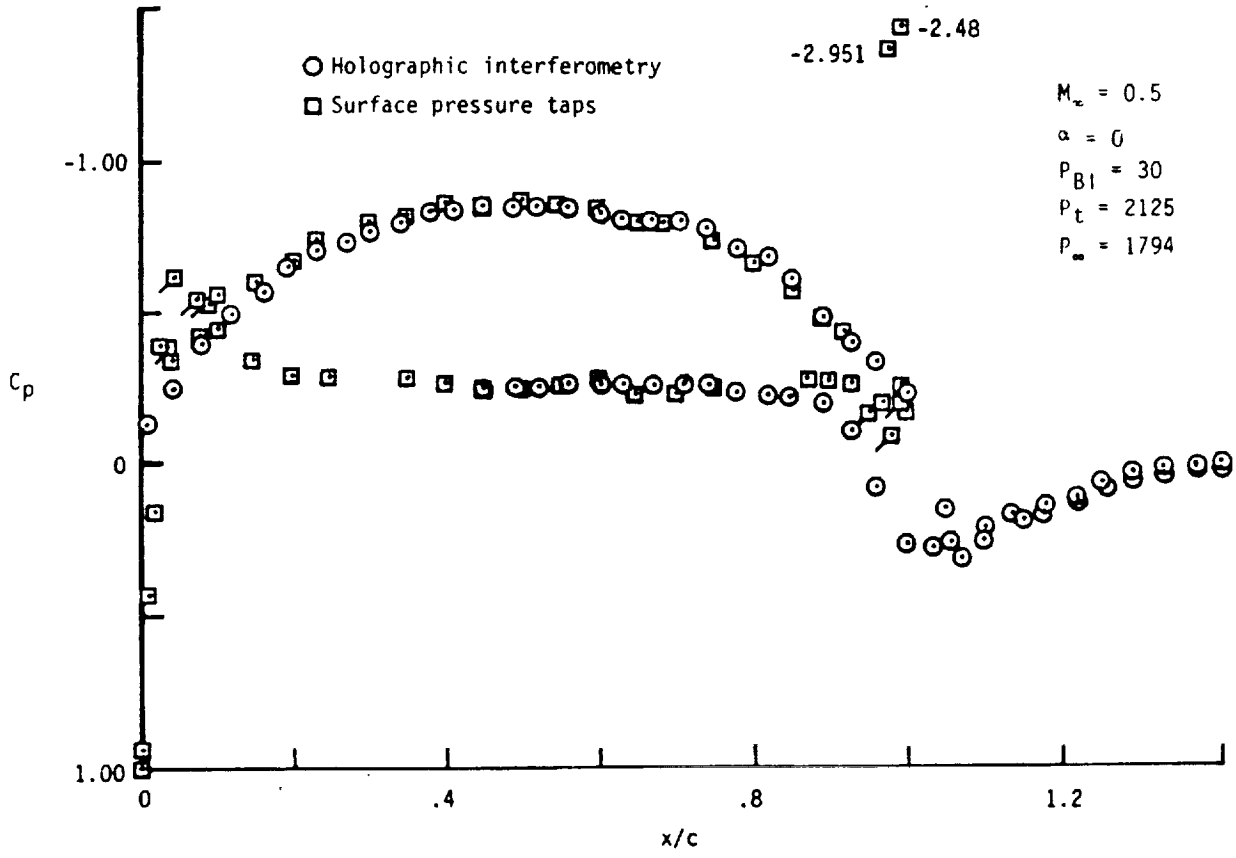

(b) P_{B1} = 30 psi

Figure 12.- Concluded.

At the leading edge, the fringes were partially masked by the support hardware so the discrepancy was to be expected. The trailing-edge pressure difference was due to the Coanda jet. Whereas the interferogram obtains the inviscid flow pressure outside of the jet, the wall taps respond to the surface pressure beneath the jet. This very large negative pressure across the jet and upper surface boundary layer and the subsequent positive pressure gradient served to turn the flow around the blunt trailing edge of the airfoil. An advantage of the interferometry technique was that the static pressures beyond the model can be determined. For example, the pressure distribution in the near-wake region was obtainable.

Although there was a pressure difference across the wake immediately downstream of the model in all cases, in the high blowing case ($M_\infty = 0.5$, $P_{B1} = 20$), the pressure difference was large. However, at $P_{B1} = 30$, the jet separated and the pressure difference across the near-wake collapsed except at the base of the model. In this case, the jet momentum was so great that the reduced surface pressure was insufficient for maintaining jet turning about the trailing edge. Note that the jet detachment resulted in a much lower pressure on the lower surface of the model.

When $M_\infty = 0.65$ (figs. 13a and b), the large negative pressure peak found at $M_\infty = 0.5$, $P_{B1} = 20$ was not apparent. At the higher Mach numbers compression waves could be seen on the upper surface of the airfoil (e.g., figs. 10a and b). These compression waves served to retard the flow in the boundary layer and resulted in a boundary-layer thickness at the jet that was two to three times greater than at $M_\infty = 0.5$. The Coanda jet was then much less effective in energizing the boundary layer and producing the negative pressures required in turning the flow about the trailing edge. Comparisons of the $M_\infty = 0.5$ and $M_\infty = 0.65$ cases at 20 psi blowing

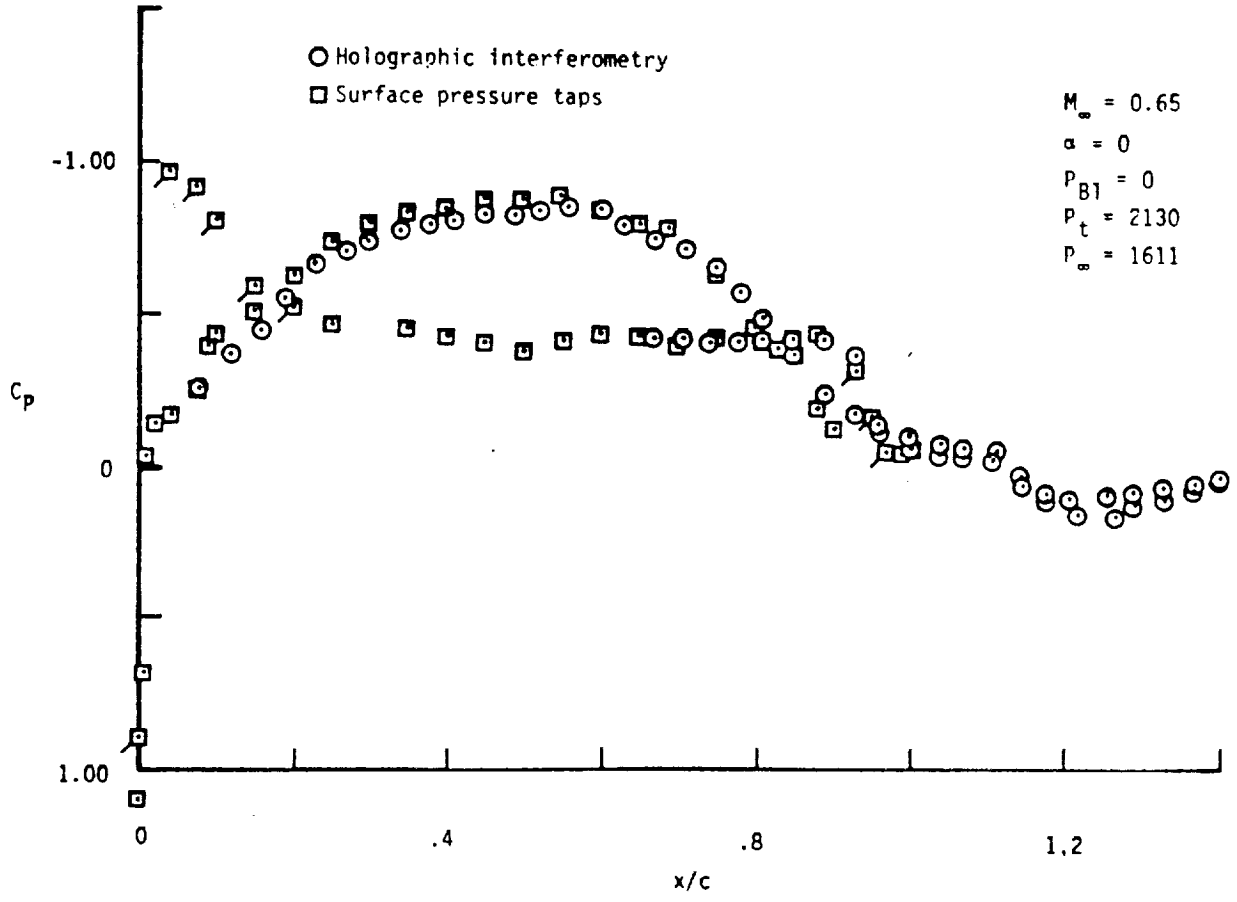

(a) P_{B_1} = 0 psi

Figure 13.- Comparisons of the measured surface pressures at M_∞ = 0.65.

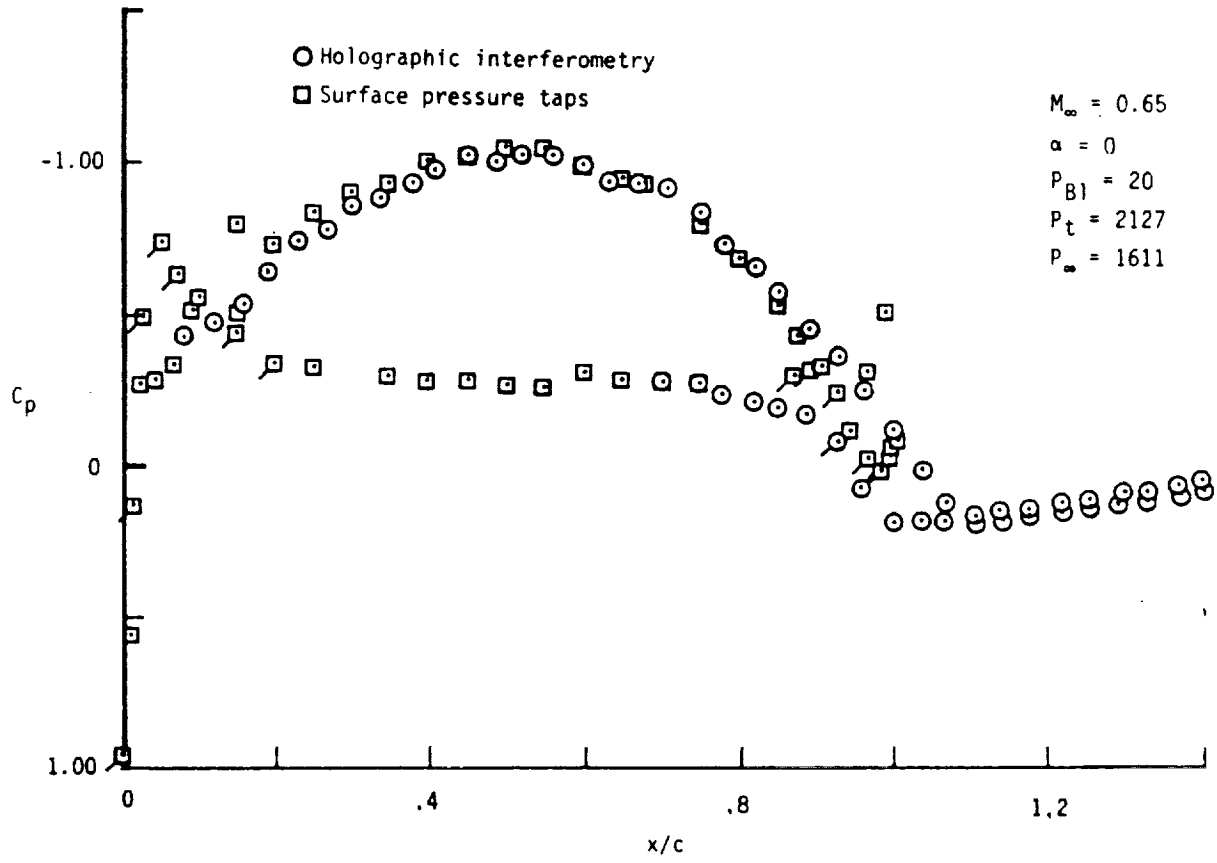

(b) P_{B1} = 20 psi

Figure 13.- Concluded.

pressures showed that the jet remained attached at the lower Mach number whereas evidence of jet separation could be seen at $M_\infty = 0.65$.

The blowups of the trailing-edge section shown in figures 14a, b, c, and d and 15a and b were useful in attempting to understand the mechanism of Coanda blowing. In interpreting these results, it should be remembered that the fringes are lines of constant density and under certain conditions, will be lines of constant flow speed. The close packing of fringes indicates strong density gradients. These gradients were especially apparent in the attached blowing cases as, for example, at $M_\infty = 0.5$, $P_{B1} = 15$. For this particular case, the attached jet can be visualized as fringes running parallel to the trailing edge. The merging of the inviscid flow fringes to the trailing edge is indicative of the strong pressure gradient there. At $M_\infty = 0.5$ and a blowing pressure of 30, the jet detachment can be seen as a local wake-like fringe pattern immediately downstream of the jet. Careful inspection shows faint fringes running parallel to the trailing edge. The inner part of the separated jet apparently was still effective in partially maintaining flow attachment.

Boundary-layer and wake-flow profiles have been computed for some representative cases (figs. 16a, b, and c). The flow speeds were computed using the Croccos relationship using the conditions at the boundary-layer edge and $T(y) = p/R\rho(y)$. Previous comparisons have been made (Bachalo[7]) with pitot probe data in the wakes of supercritical airfoils and demonstrated very good agreement. Thus, these data have reasonable reliability, although direct comparisons to laser velocimeter or pitot profiles would have been useful.

The wake data were useful in determining the character of the viscous flow and have the potential of providing drag data. In addition, the

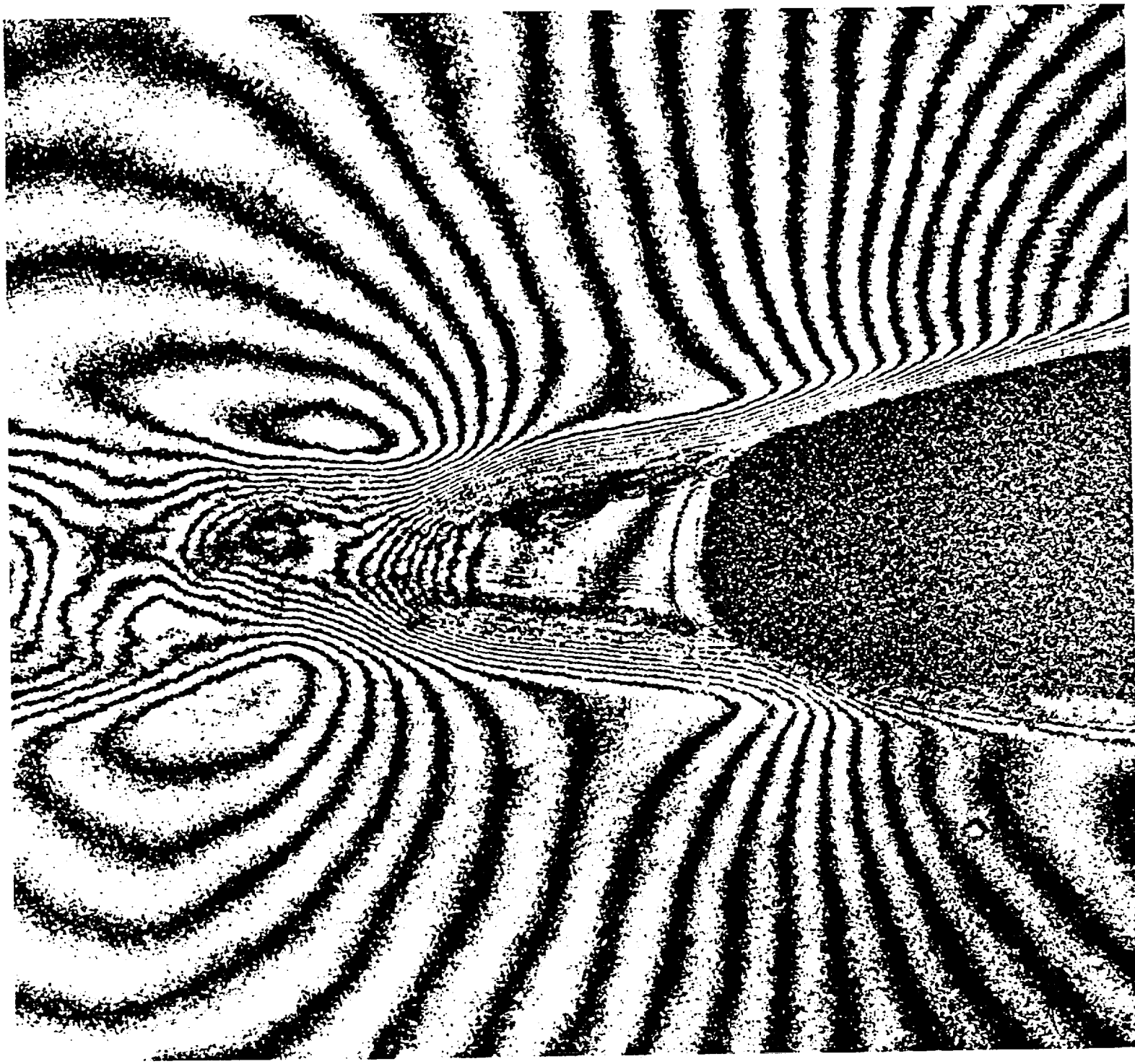

(a) P_{B1} = 0 psi

Figure 14.- Enlarged views of the trailing-edge region at M_∞ = 0.5.

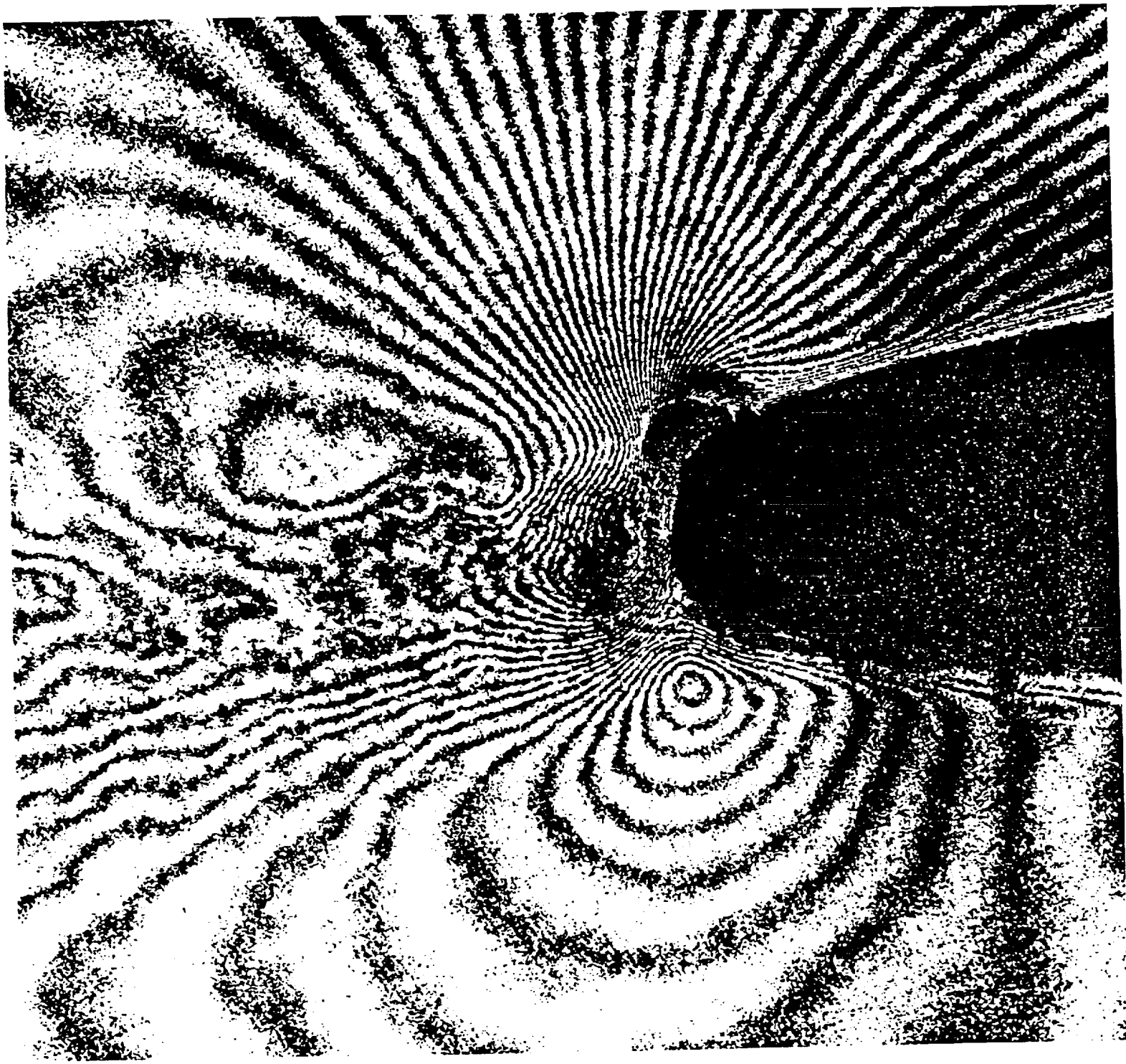

(b) P_{B1} = 15 psi

Figure 14.- Continued.

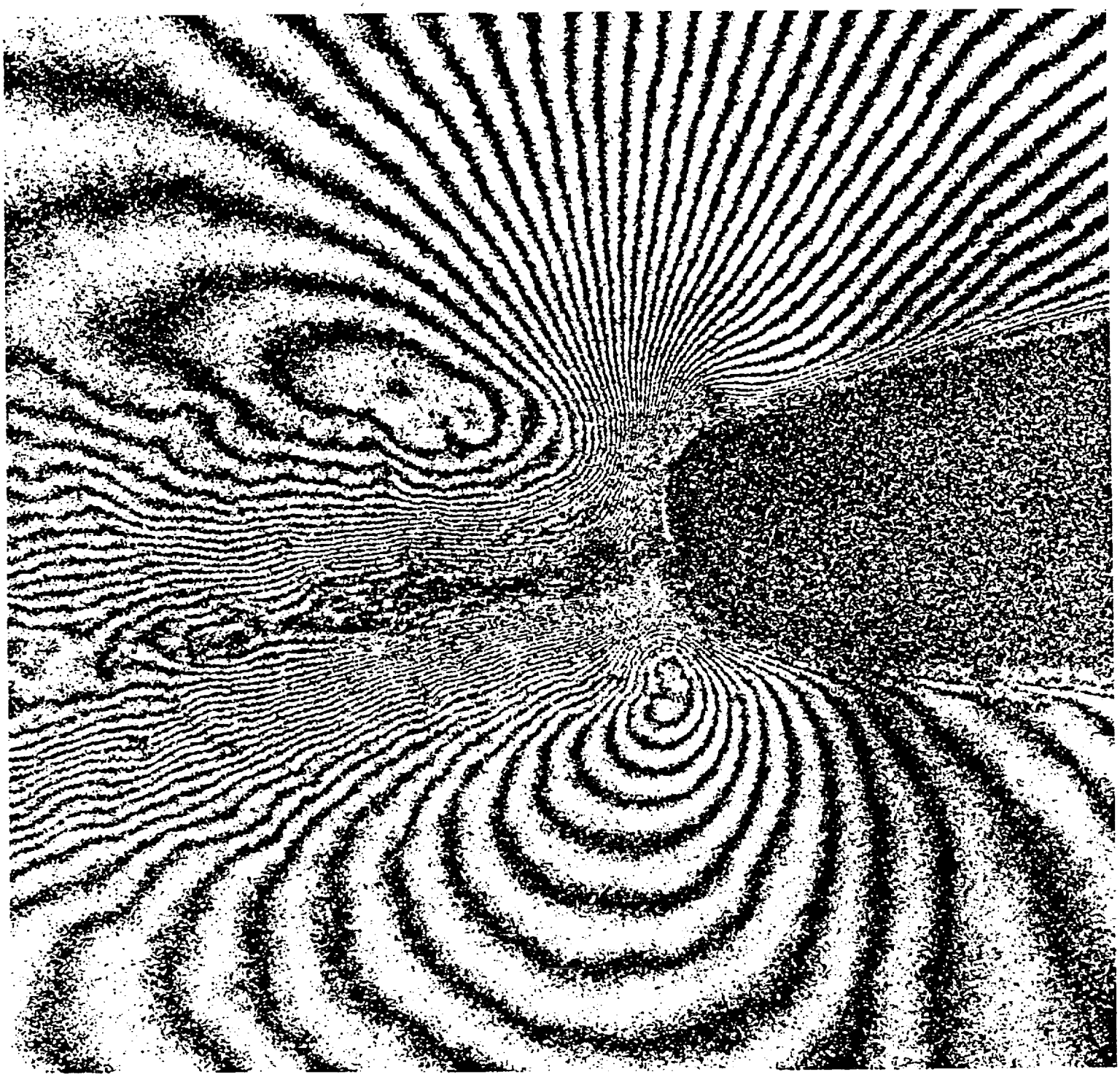

(c) P_{B1} = 20 psi

Figure 14.- Continued.

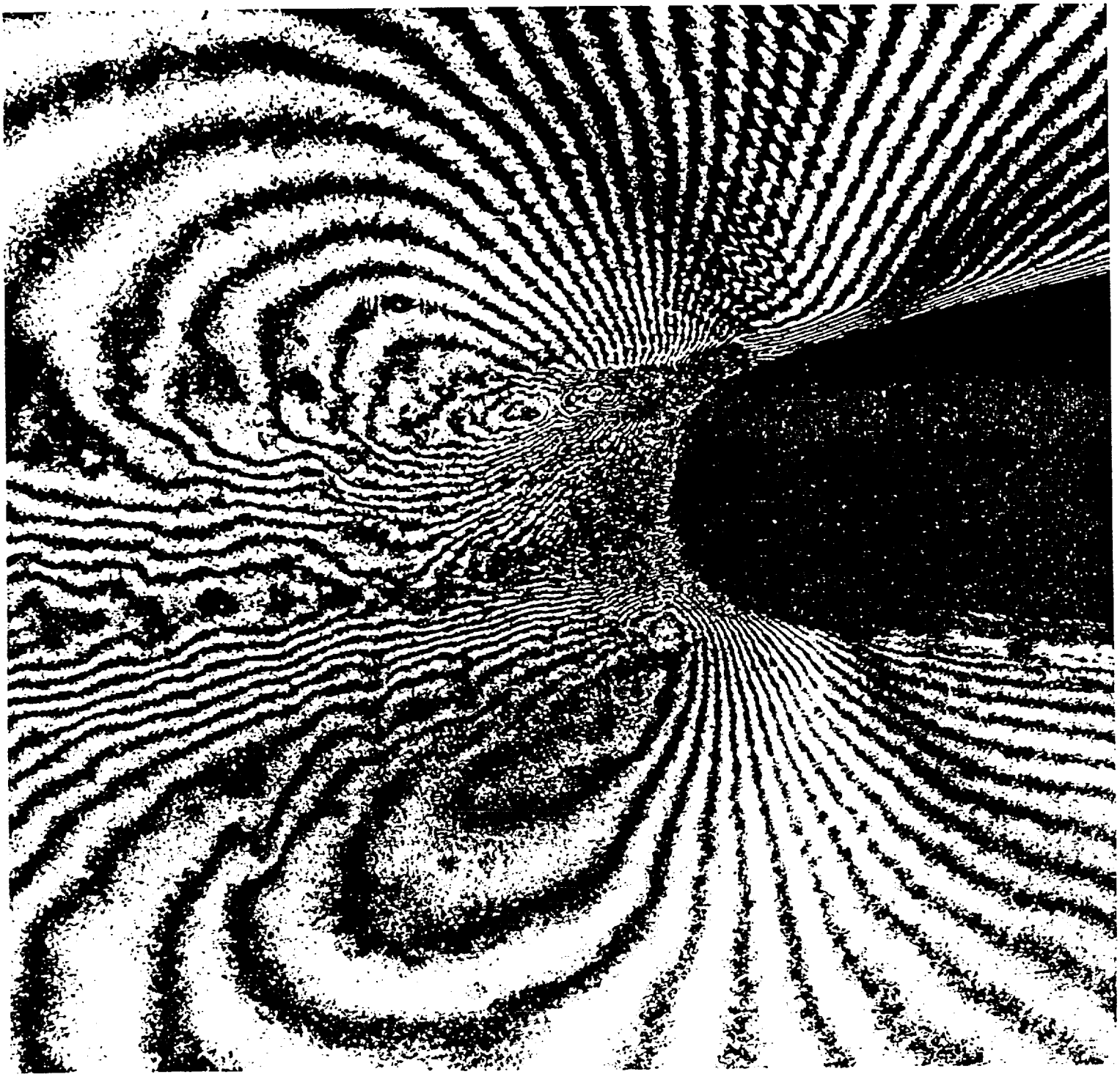

(d) P_{B1} = 30 psi

Figure 14.- Concluded.

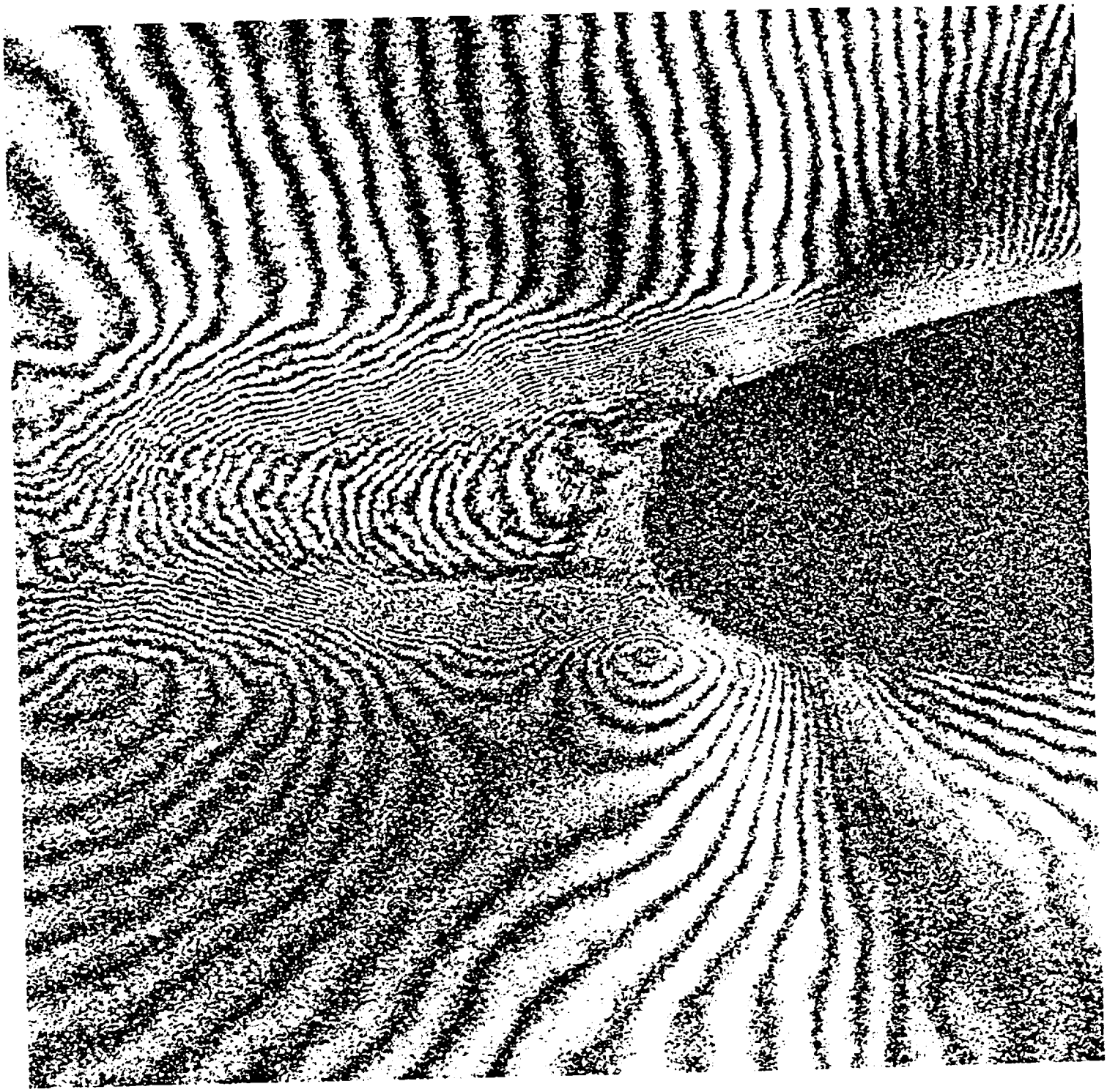

(a) P_{B1} =10 psi

Figure 15.- Enlarged views of the trailing-edge region at $M_\infty = 0.7$

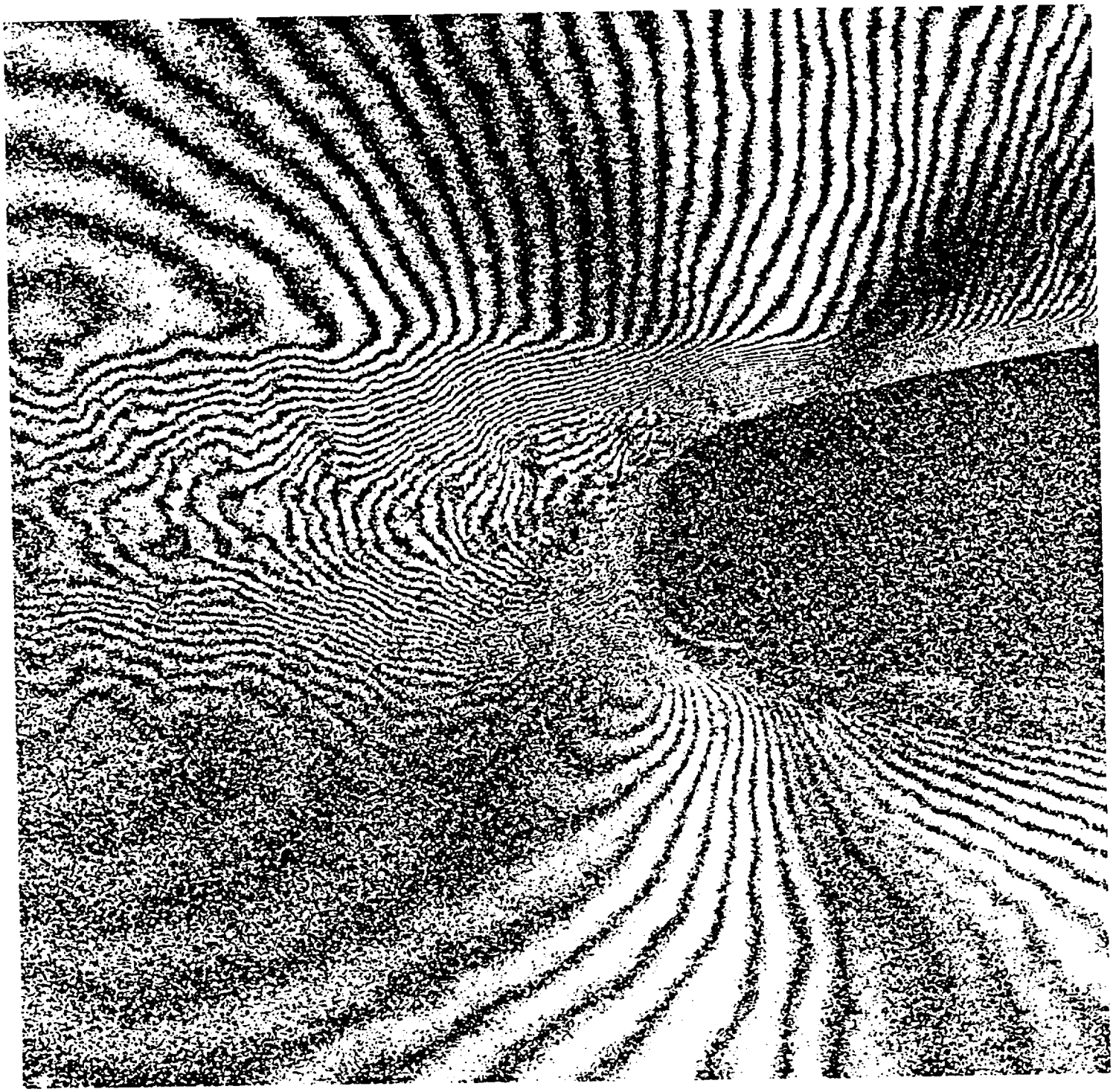

(b) P_{B1} = 20 psi

Figure 15.- Continued.

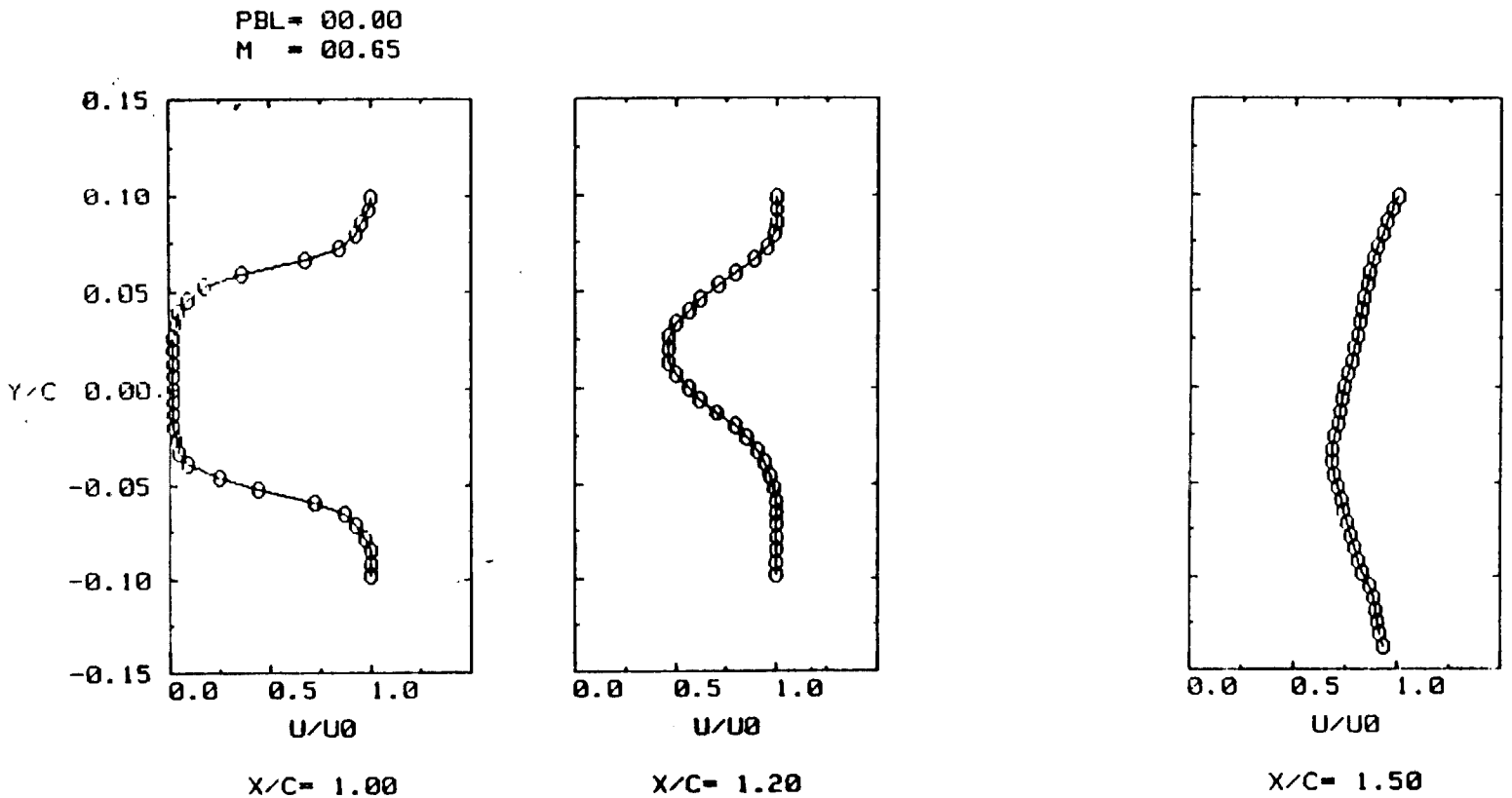

(a) P_{B1} = 0 psi

Figure 16.- Wake profiles obtained from the interferograms at M_∞ = 0.65.

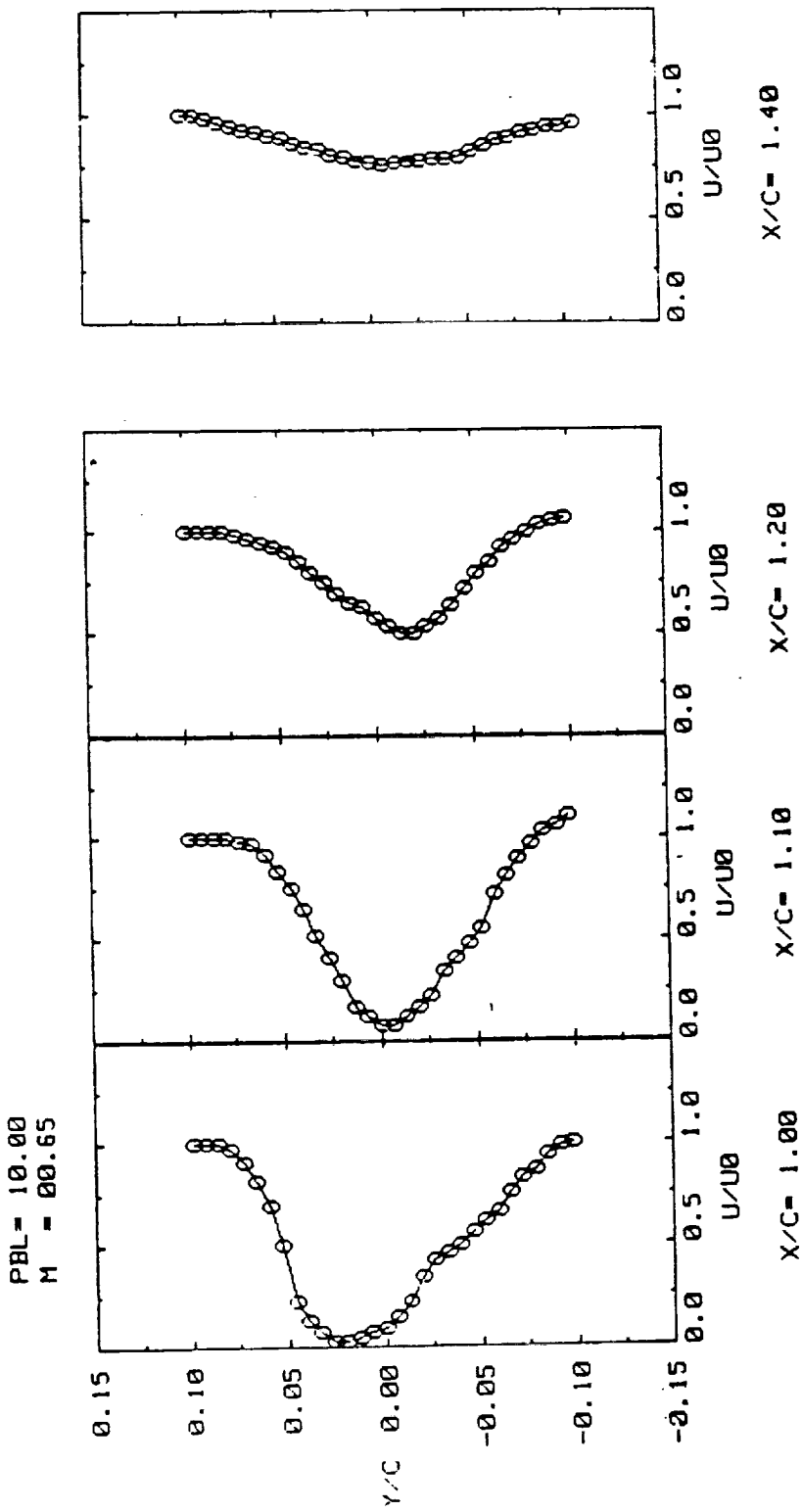

(b) P_{B1} = 10 psi

Figure 16.- Continued.

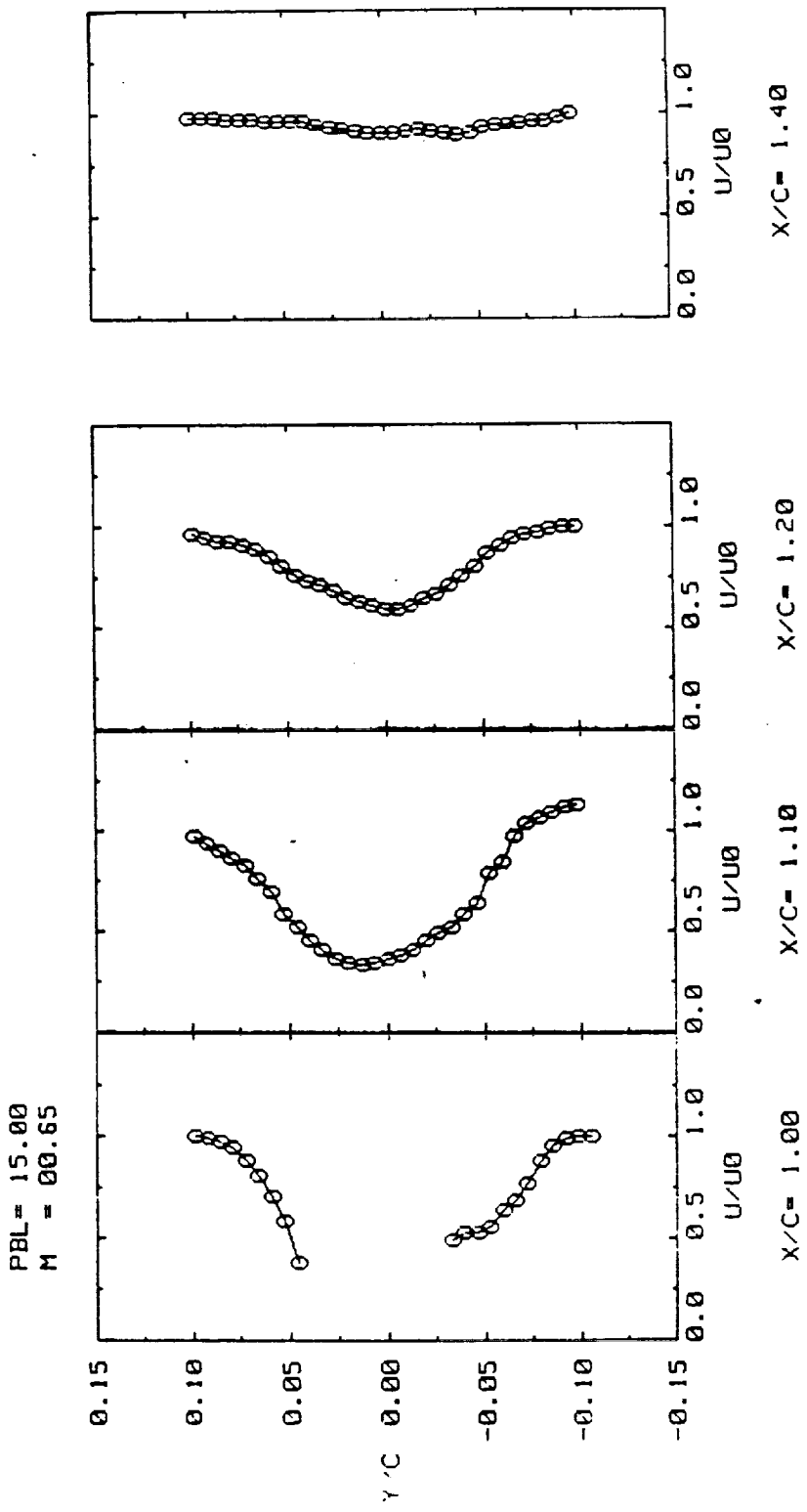

(c) P_{B1} = 15 psi

Figure 16.- Concluded.

flow direction in the wake obtained from a trace of the minimum velocity points can be used to estimate the apparent lift produced by the airfoil. Because of the vortices produced at the wind-tunnel sidewalls, an additional downwash can be expected. The extent of this three-dimensional flow can be estimated from the lift measured from the wake flow angle compared to the lift obtained from the integration of the pressure distribution.

4.0 SUMMARY AND CONCLUSIONS

Results have been presented for the flow about a circulation control airfoil at transonic flow speeds. The interferometry technique used provided both detailed flow visualization and quantitative data. Surface pressure results obtained from the interferograms agreed reasonably well with the measured surface pressures. This provided some reassurance that the interferometer system was not significantly affected by any three-dimensionality of the flow.

In addition, since the interferometer obtained the pressure at the outer edge of the viscous layer, the pressure across the jet, for example, could be obtained. Also, pressures beyond the airfoil trailing edge could be measured. These results have the potential for further evaluation of the effectiveness of the Coanda blowing.

The key result is the ability to correlate the extent of the jet separation with the drop in C_ℓ. Also, the increased thickness of the upper surface boundary layer caused by compression or weak shock waves was found to correlate with a reduction in the maximum C_ℓ achieved.

Although time was not available to perform a complete analysis, it is apparent that the drag may be obtained from the wake profiles. Furthermore, the wake deflection angle can be estimated with sufficient accuracy to obtain the lift. This determination of the lift may, however, be affected by the vortices induced at the sidewalls. Comparisons should be made to integrated pressure distributions.

These results have provided a good deal of information on the character of the flow field, particularly in the neighborhood of the trailing edge. Future work should be concentrated on obtaining more detailed information on the flow in the neighborhood of the jet. This

can be achieved using the existing system but would be better served with specially-designed optics. The poor quality of the holograms which resulted from the bad film may have caused some loss of detail in the trailing edge of the airfoil.

As to the airfoil design, it is apparent that improved performance can be achieved if the jet detachment is delayed. One possible way of achieving this is by expanding the jet to supersonic speed before it interacts with the airfoil boundary layer. This will serve to reduce the density while increasing the velocity. Another design improvement would involve the development of an optimum trailing-edge shape for the expected operating Mach and Reynolds number ranges. Clearly, a great deal of research is required to properly establish a knowledge base for full-scale model development.

REFERENCES

1. Wood, N. J., "The Aerodynamics of Circulation Control Aerofoils," Joint Institute for Aeronautics and Acoustics, Stanford University, TR-41, July 1981.
2. Englar, R. J., "Two-Dimensional Transonic Wind-Tunnel Tests of Three 15-Percent-Thick Circulation Control Airfoils," Naval Ship Research and Development Center, Technical Note AL-182, December 1970.
3. Englar, R. J., "Experimental Investigation of the High Velocity Coanda Wall Jet Applied to Bluff Trailing-Edge Circulation Control Airfoils," David W. Taylor Naval Ship Research and Development Center, Report 4708, September 1975.
4. Ottensoser, J., "Two-Dimensional Subsonic Evaluation of a 15-Percent-Thick Circulation Control Airfoil With Slots at Both Leading and Trailing Edges," Naval Ship Research and Development Center, Report 4456, July 1974.
5. Abramson, Jane, "Two-Dimensional Subsonic Wind-Tunnel Evaluation of a 20-Percent-Thick Circulation Control Airfoil," David W. Taylor Naval Ship Research and Development Center, Report ASED 311,1975
6. Wood, N. and Conlon, J., "The Performance of a Circulation Control Aerofoil at Transonic Speeds", Paper 83-0083, Presented at AIAA 21st Aerospace Sciences Meeting, Reno 1983.
7. Bachalo, W. D., "Measurements of Supercritical Airfoil Flow Fields Using Interferometry," Final report for Douglas Aircraft Company, Long Beach, March 22, 1982.

FIGURES

Figure 1.- Schematic of the circulation control model.

Figure 2.- Transmitting stage schematic of the 2- by 2-ft holographic interferometer.

Figure 3.- Receiving stage schematic of the 2- by 2-ft holographic interferometer.

Figure 4.- Reconstruction system schematic.

Figure 5.- Interferograms of the flow field at $M_\infty = 0.5$, $\alpha = 0°$.

(a) $P_{B1} = 0$ psi

(b) $P_{B1} = 15$ psi

(c) $P_{B1} = 20$ psi

(d) $P_{B1} = 25$ psi

(e) $P_{B1} = 30$ psi

Figure 6.- Interferograms of the flow field at $M_\infty = 0.5$, $\alpha = -5°$.

(a) $P_{B1} = 0$ psi

(b) $P_{B1} = 10$ psi

(c) $P_{B1} = 15$ psi

(d) $P_{B1} = 20$ psi

(e) $P_{B1} = 30$ psi

Figure 7.- Plot of lift coefficient with blowing at a range of freestream Mach numbers.

Figure 8.- Schematic of the trailing-edge flow field.

(a) Attached jet.

(b) Detached jet.

Figure 9.- Interferograms of the flow field at $M_\infty = 0.6$, $\alpha = 0$.

(a) $P_{B1} = 0$ psi

(b) $P_{B1} = 10$ psi

(c) P_{B1} = 12 psi

(d) P_{B1} = 15 psi

(e) P_{B1} = 17 psi

Figure 10.- Interferograms of the flow field at M_∞ = 0.65.

(a) P_{B1} = 0 psi

(b) P_{B1} = 10 psi

(c) P_{B1} = 15 psi

(d) P_{B1} = 20 psi

(e) P_{B1} = 30 psi

Figure 11.- Interferograms of the flow field at M_∞ = 0.7.

(a) P_{B1} = 0 psi

(b) P_{B1} = 10 psi

(c) P_{B1} = 20 psi

Figure 12.- Comparisons of the measured surface pressures at M_∞ = 0.5.

(a) P_{B1} = 20 psi

(b) P_{B1} = 30 psi

Figure 13.- Comparisons of the measured surface pressures at M_∞ = 0.65.

(a) P_{B1} = 0 psi

(b) P_{B1} = 20 psi

Figure 14.- Enlarged views of the trailing-edge region at M_∞ = 0.5.

(a) P_{B1} = 0 psi

(b) P_{B1} = 15 psi

(c) P_{B1} = 20 psi

(d) P_{B1} = 30 psi

Figure 15.- Enlarged views of the trailing-edge region at M_∞ = 0.65.

(a) P_{B1} = 0 psi

(b) P_{B1} = 20 psi

(c) P_{B1} = 30 psi

Figure 16.- Wake profiles obtained from the interferograms at $M_\infty = 0.65$.

(a) $P_{B1} = 0$ psi

(b) $P_{B1} = 10$ psi

(c) $P_{B1} = 15$ psi